J. Fluid Mech. (1998), *vol.* 356, *pp.* 155–197. Printed in the United Kingdom

Square cells in surface-tension-driven Bénard convection: experiment and theory

By KERSTIN ECKERT[1], MICHAEL BESTEHORN[2] AND ANDRÉ THESS[1]

[1] Center for Physical Fluid Dynamics, Department of Mechanical Engineering,
Dresden University of Technology, 01062 Dresden, Germany

[2] Institute for Theoretical Physics and Synergetics, University of Stuttgart,
Pfaffenwaldring 57/4, 70550 Stuttgart, Germany

(Received 7 June 1996 and in revised form 8 September 1997)

The convective flow in a thin liquid layer with a free surface heated from below is studied using a combination of accurate experiments with silicone oil ($\nu = 0.1$ cm^2 s^{-1}) and high-resolution direct numerical simulations of the time-dependent governing equations. It is demonstrated that above a certain value ε_s of the threshold of primary instability, $\varepsilon = 0$, square convection cells rather than the seemingly all-embracing hexagons are the persistent dominant features of Bénard convection. The transition from hexagonal to square cells sets in via a subcritical bifurcation and is accompanied by a sudden rapid increase of the Nusselt number. This implies that square cells are the more efficient mode of heat transport. Their wavenumber exceeds that of hexagonal cells by about 8%. The transition depends on the Prandtl number and it is shifted towards higher ε_s if the Prandtl number is increased. The replacement of hexagonal by square cells is mediated by pentagonal cells. In the transitional regime from hexagonal to square cells, characterized by the presence of all three planforms, the system exhibits complex irregular dynamics on large spatial and temporal scales. The time dependence becomes more vivid with decreasing Prandtl number until finally non-stationary square cells appear. The simulations agree with the experimental observations in the phenomenology of the transition, and in the prediction of both the higher Nusselt number of square Bénard cells and the subcritical nature of the transition. Quantitative differences occur with respect to the values of ε_s and the Prandtl number beyond which the time dependence vanishes. These differences are the result of a considerably weaker mean flow in the simulation and of residual inhomogeneities in the lateral boundary conditions of the experiment which are below the threshold of control.

1. Introduction

Since the first experiments of Henri Bénard (Bénard 1900), surface-tension-driven convection in shallow liquid layers has been identified with the hexagonal planform, partially due to the suggestive power of aesthetic hexagonal patterns, and mostly due to the absence of reliable experimental and theoretical studies, extending sufficiently far into the nonlinear regime. The purpose of the present paper is to utilize a symbiotic combination of laboratory experiments and direct numerical simulation to advance the understanding of convection in high-Prandtl-number fluids when surface tension forces dominate buoyancy. Such flow is referred to as surface-tension-driven Bénard convection, henceforth abbreviated as STDBC. The main result of our work is the observation and characterization of square convective cells that appear, beyond a certain distance from the instability threshold, as a new intrinsic planform of STDBC. Preliminary accounts of the present work have been given by Nitschke-Eckert & Thess (1995) and by Bestehorn (1996).

Studies on pattern formation and turbulence driven by temperature gradients were focused, until the present day, mainly on buoyancy-driven Rayleigh–Bénard convection (RBC). For this system a rather comprehensive understanding has been reached in the last years. It comprises the pattern formation in the infinitely extended system, formulated in Busse's extensive theory (Busse 1981 and references therein) and supported by various experiments (Krishnamurti 1970; Busse & Whitehead 1971, 1974), as well as the scaling properties of the Nusselt number over a range of more than 16 decades of $\varepsilon = (\Delta T - \Delta T_c)(\Delta T_c)$. ($\Delta T_c$ is the temperature difference required for onset of convection.) For an overview see e.g. the review article of Siggia (1994).

In comparison with RBC the experimental and theoretical results in the field of STDBC are more sparse. Below we shall review the existing body of work from a special point of view, namely up to which value of ε the studies have been extended and what their results were with respect to pattern selection. For a detailed overview of STDBC we refer to Velarde & Castillo (1982), Koschmieder (1993) and Simanovskii & Nepomnyashchy (1993).

Let us now consider in which way experimental work has developed our present knowledge of Bénard convection. Based on his experiments ($\varepsilon \ll 1$), Block (1956) provided evidence that surface tension variations rather than density variations are the driving force of Bénard convection. The systematic exploration of the weakly supercritical range, i.e. $0 \leqslant \varepsilon \leqslant 0.5$, started in the late sixties. Pearson's (1958) theory with respect to the critical wavenumber has been verified by Koschmieder (1967). The critical temperature difference for onset of convection, predicted by a generalization of Pearson's theory with respect to buoyancy (Nield 1964), was confirmed by Palmer & Berg (1971). Later precise experiments by Koschmieder & Biggerstaff (1986) in very thin layers showed motions far below the critical temperature difference of Pearson's theory, and are unexplained up to now. The subcritical onset of STDBC, finally, has been explored in a recent work by Schatz *et al.* (1995). Another important feature, namely the surface depression in the centre of the hexagonal cell, was confirmed by Cerisier *et al.* (1984). Further we should mention the experiments regarding the pattern selection in small-aspect-ratio cells $\Gamma \sim 1$ (Koschmieder & Prahl 1990; Ondarçuhu *et al.* 1993; Mindlin *et al.* 1994). These experiments reveal patterns in the form of rolls, circular segments, triangular and square cells. Their selection, however, is forced by the influence of the lateral walls.

For the moderately supercritical range, i.e. $\varepsilon \sim 1$, Koschmieder (1991) and Koschmieder & Switzer (1992) demonstrated that the decrease of the size of the hexagons with increase of ε is an intrinsic feature of STDBC in the range $\varepsilon \leqslant 1$. At higher supercriticality ε this decrease is reversed to a monotonic increase of the cell size (Cerisier *et al.* 1987*b*) as is also known from RBC. Another topic of interest is the stability of different planforms in STDBC. Cerisier *et al.* (1987*a*) showed that hexagons lose the competition with rolls at a certain distance from the instability threshold if the depth of the liquid layer is increased.

To summarize the experimental efforts, we note that most of the experiments are restricted to hexagonal convection in the immediate vicinity of the instability threshold. Pattern selection for small aspect ratios ($\Gamma < 10$), which leads partly to non-hexagonal planforms, is exclusively determined by the influence of the walls and gives no information regarding the intrinsic stability of hexagons in extended systems. At the highest value of $\varepsilon \sim 7$ achieved for aspect ratios $\Gamma \gg 10$ (Cerisier *et al.* 1987*b*), however, under the condition of a non-controlled gas layer and with perturbation of the free surface, no indication regarding the existence of a secondary instability has been found. Caused by the high Prandtl number of 880, hexagons were still the dominant planform, although their degree of order was reduced.

On the theoretical side, both the absence of reflection symmetry with respect to the midplane of the layer and the location of the driving force at the free surface are sources of an increased complexity of STDBC in comparison with RBC. The linear stability problem, i.e. $\varepsilon = 0$, was explored for the first time by Pearson (1958). Later, Nield (1964) included the combined effect of surface tension and buoyancy. The studies of nonlinear STDBC can be grouped into bifurcation analysis based on amplitude equations (Scanlon & Segel 1967; Cloot & Lebon 1984; Bragard & Lebon 1993; Bestehorn 1993; Parmentier, Regnier & Lebon 1996; Golovin, Nepomnyashchy & Pismen 1997; Regnier *et al.* 1997), and into direct numerical simulations of the governing equations (Bestehorn 1993, 1996; Thess & Orszag 1995; Yu, Jiang & Duh 1996; Dauby & Lebon 1996).

The first attempt to understand weakly nonlinear Bénard convection by means of bifurcation analysis originates from Scanlon & Segel (1967). Their theory, developed for the case of infinite Prandtl number, predicts the selection of hexagonal cells in favour of rolls above the onset of STDBC. The theory of Scanlon & Segel was refined and partially corrected by Cloot & Lebon (1984), Bragard & Lebon (1993) and Parmentier *et al.* (1996). All these works predict the same hierarchy of transitions with increasing ε starting with hexagons at onset, passing through a mixed state of hexagons and rolls, and, finally, terminating in a pure roll state. Motivated by previous experiments of the present authors (Nitschke-Eckert & Thess 1995), these papers have been generalized by two recent works making allowance for square cells as a possible solution. Golovin *et al.* (1997) developed a weakly nonlinear theory for the complete liquid-gas-Bénard system. They point out that in certain ranges of the gas-to-liquid depths ratio and the ratio of gas to liquid heat conductivities square cells do indeed become the stable solution. Regnier *et al.* (1997) studied the one-layer system under the influence of buoyancy. They determined the critical ratio between surface tension and buoyancy as a function of material parameters beyond which square cells are the preferred planform. Both works stress the importance of both the heat transfer at the free surface and the liquid viscosity on the selection of square cells. Their predictions are in qualitative agreement with the results of the present and foregoing papers, bearing in mind the limited validity of amplitude equation models for $\varepsilon > 1$.

The first direct numerical simulation of three-dimensional STDBC for medium aspect ratios ($\Gamma \sim 30$) was performed by Bestehorn (1993). In combination with an amplitude equation analysis it gives a rather comprehensive picture of the phase and amplitude instabilities in the weakly supercritical STDBC. However, the code used was restricted to liquids with an infinite Prandtl number. It was later extended to the case of finite Prandtl number by inclusion of the toroidal part of the velocity field (Bestehorn 1996) and serves as one basis of the present paper. In recent works Yu *et al.* (1996) and Dauby & Lebon (1996) were able to reproduce with high precision the planform selection, as it takes place at small aspect ratios in the weakly supercritical range (see Koschmieder & Prahl 1990). The only simulation that covers the strongly nonlinear range of STDBC up to $\varepsilon = 24$ in a small-aspect-ratio box ($\Gamma \sim 1$) was undertaken by Thess & Orszag (1995). It revealed universal small-scale features of the temperature field. The latter simulation, performed at a larger aspect ratio, as well as the simulation of Bestehorn (1993), was able to reproduce the correct wavenumber dependence on ε in the weakly supercritical range of STDBC.

The foregoing review makes it clear that the range of supercriticality ε, accessible up to now for large-aspect-ratio STDBC, is smaller than one decade in magnitude, which is far below the range in RBC. Why is this so? Although the existing codes can handle in principle aspect ratios up to $\Gamma \sim 40$, the integration time necessary to get far enough into the nonlinear regime is beyond the capabilities of present computers. The experimental reason for this narrow ε-range is that the requirement of small layer depth, necessary for the dominance of surface tension forces over buoyancy, imposes severe constraints on the maximum of supercriticality, as shown later on.

In the present paper we extend both the measurements of Koschmieder & Biggerstaff (1986) and Koschmieder & Switzer (1992) and the existing numerical results up to $\varepsilon \sim 8$. This allows us to study in detail the nonlinear evolution of the hexagonal pattern. We demonstrate that STDBC is not exhausted with the generation of hexagonal convection cells. Moreover, the system is capable of developing patterns with a square symmetry connected with a complex spatio-temporal dynamics. In fact, STDBC seems to be able to extend our ideas on pattern formation in a way that is similar to that done recently by the observation of spiral-defect chaos in the RBC case (Morris *et al.* 1993).

The paper is organized as follows. In §2 we give a brief introduction to the liquid–gas Bénard system in the form to which both the experiment and the numerical simulation refer. We explain the physical mechanism and present the governing equations. Section 3 contains a detailed description of the approaches by which the system is analysed in the experiment and in the numerical simulation. In §§4–6 we present the results in the form of the essential physical features which accompany the replacement of hexagonal by square convection cells in STDBC. In §4 we deal with the geometrical aspects of this transition. We study the changes in the composition of the structure and look into the characteristic lengths of cells of a particular planform. The influence of the Prandtl number on the transition is illuminated. Section 5 is devoted to the investigation of the efficiency of cells of different planform in the transport of heat. Both the Nusselt number and temperature differences inside a cell are examined. Furthermore, the hysteresis accompanying the transition is studied. In §6 we report the complex spatio-temporal behaviour connected with the transition. The results are summarized in §7.

2. The liquid–gas Bénard system

2.1. *Governing equations*

The system under consideration is sketched in figure 1. A layer of liquid is heated from below by a horizontal plate which is of a uniform temperature. The free surface of the liquid is in contact with a gas, cooled by the upper isothermal plate. The quiescent basic state of the liquid–gas system loses its stability once the temperature difference between the lower and the upper plate exceeds a critical value. In general, the instability and the resulting cellular convection is driven by two effects, namely buoyancy and surface tension. We are interested in situations where the influence of surface tension dominates buoyancy. Under terrestrial conditions this parameter range is realized in liquid layers with thickness of the order of 1 mm or less. This

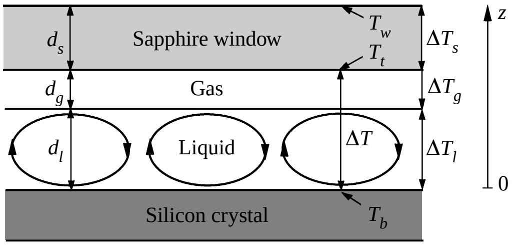

FIGURE 1. Schema of the liquid–gas Bénard system: a temperature difference ΔT is maintained across a two-layer system by isothermal plates. The flow is exclusively driven by the temperature dependence of surface tension whereby the deflection of the free surface is neglected. The auxilary variables ΔT_l and ΔT_g represent the average temperature drop in the liquid and in the gas, respectively. They are defined in §3.1.2. d_l and d_g are the thicknesses of the respective layers.

type of flow is referred to as surface-tension-driven Bénard convection. The most important ingredient of STDBC is the fact that the surface tension σ is a function of the temperature T. We assume the linear relationship

$$\sigma = \sigma_0 - \gamma(T - T_b), \tag{2.1}$$

where the temperature coefficient of the surface tension $\gamma = -\mathrm{d}\sigma/\mathrm{d}T$ is positive for the liquid used in the experiments. We briefly recall the basic physical mechanism of STDBC. If a hot spot is generated at the free surface due to a temperature fluctuation, the surface tension is lowered according to equation (2.1). As a result, liquid is pulled radially outward to the region of high surface tension. By continuity, this causes upflow in the vicinity of the spot. For a sufficiently strong basic temperature gradient the upwelling hot liquid reinforces the temperature disturbance and gives rise to instability. Convection occurs. While the weakly nonlinear regime is well understood, the behaviour in the strongly nonlinear regime of STDBC has not received comprehensive analysis. The study of this regime is the main purpose of the present work. We chose the two-layer system as the 'canonical problem', rather than the more familiar one-layer system, since the former is free of any *ad-hoc* assumptions about the mechanism of heat transfer at the free surface. We focus on a system in which the surface deflection caused by convective motion is negligible.

The system defined in figure 1 is governed by the incompressible Navier–Stokes equation

$$\partial_t \boldsymbol{v}_i + \boldsymbol{v}_i \cdot \nabla \boldsymbol{v}_i = -\frac{1}{\rho_i}\nabla p_i + \nu_i \Delta \boldsymbol{v}_i, \tag{2.2}$$

$$\nabla \cdot \boldsymbol{v}_i = 0, \tag{2.3}$$

and by the energy equation

$$\partial_t T_i + \boldsymbol{v}_i \cdot \nabla T_i = \kappa_i \Delta T_i \tag{2.4}$$

for each phase *i*, where $i = l[i = g]$ refers to the liquid [gas]. Assuming that the liquid and gas have the thickness d_l and d_g, respectively, we can formulate the following boundary and matching conditions. At the bottom $z = 0$,

$$\boldsymbol{v}_l = 0, \;\; T_l = T_t + \Delta T. \tag{2.5}$$

At the free surface $z = d_l$ we impose

$$v_l^{(x)} = v_g^{(x)}, \qquad v_l^{(y)} = v_g^{(y)}, \qquad v_l^{(z)} = 0, \qquad v_g^{(z)} = 0, \tag{2.6}$$

$$T_l = T_g, \tag{2.7}$$

$$\lambda_l \partial_z T_l = \lambda_g \partial_z T_g, \tag{2.8}$$

$$\rho_l \nu_l \partial_z v_l^{(x)} - \rho_g \nu_g \partial_z v_g^{(x)} = -\gamma \partial_x T_l, \qquad \rho_l \nu_l \partial_z v_l^{(y)} - \rho_g \nu_g \partial_z v_g^{(y)} = -\gamma \partial_y T_l. \tag{2.9}$$

At the top plate $z = d_l + d_g$ the conditions are

$$\boldsymbol{v}_g = 0, \; T_g = T_t. \tag{2.10}$$

These relations express the no-slip condition and the fixed temperature ((2.5) and (2.10)) at the heating and cooling plates, and the continuity of velocity (2.6), temperature (2.7), and heat flux (2.8) across the interface. The Marangoni boundary condition (2.9) is responsible for the motion of the liquid due to non-uniformities of the temperature. The set of equations and boundary conditions (2.2)–(2.10) represents a straightforward generalization of the one-layer equations (see e.g. Davis 1987). It describes the velocity, pressure, and temperature fields in both phases as a function of space and time. The canonical problem contains twelve physical parameters, namely $\rho_i, \nu_i, \kappa_i, \lambda_i, \gamma, \Delta T, d_l, d_g$, representing the density, kinematic viscosity, thermal diffusivity, heat conductivity, temperature coefficient of surface tension, temperature difference, liquid thickness, and gas thickness, respectively. Upon introducing dimensionless variables, these parameters can be grouped into seven non-dimensional quantities. These are the ‘total’ liquid Marangoni number

$$M_{tot} = \frac{\gamma \beta_{tot} d_l^2}{\kappa_l \nu_l \rho_l}, \tag{2.11}$$

where

$$\beta_{tot} = \frac{T_b - T_t}{d_l + d_g} = \frac{\Delta T}{d_l + d_g}, \tag{2.12}$$

the Prandtl numbers of the liquid and the gas,

$$Pr_l = \frac{\nu_l}{\kappa_l}, \qquad Pr_g = \frac{\nu_g}{\kappa_g},$$

as well as the ratios ρ_g/ρ_l, κ_g/κ_l, λ_g/λ_l, d_g/d_l. The rest of the paper is devoted to the construction and analysis of laboratory and numerical models approximating the canonical problem (2.2)–(2.10).

2.2. *Definition of control parameter and Nusselt number in the two-layer-system*

To define supercriticality, and the Nusselt number of the liquid layer in the two-layer system, one can follow two different concepts, because of the existence of two scales for the temperature drop across the liquid layer: alternatively to the average temperature difference ΔT_l one is provided with the conductive temperature drop ΔT_{cd}. These quantities are given by (cf. §3.1.2)

$$\Delta T_{cd} = \frac{Bi}{1 + Bi} \, (T_b - T_t), \tag{2.13}$$

$$\Delta T_l = T_b - T_t - \frac{d_g}{\lambda_g} \frac{q}{A} \tag{2.14}$$

where q and A stand for heat flux and the area of the layer. The Biot number Bi is given by

$$Bi = \frac{\lambda_g \, d_l}{\lambda_l \, d_g} \tag{2.15}$$

(cf. §3.2.3). To correctly interpret our results, the differences between both scales needs to be recognized. The conductive temperature drop ΔT_{cd} assumes that both liquid and gas layers are in conduction, independent of the actual value of ΔT. Therefore, with the onset of convection in the liquid, ΔT_{cd} refers to a fictional system. The advantage of ΔT_{cd}, however, is the possibility of external control by varying ΔT. Thus, it can serve as the control parameter for both experiment and simulation. ΔT_l is the actual average temperature difference across the liquid layer taking liquid convection into account. The disadvantage of ΔT_l is that it cannot be controlled externally, since it changes with ΔT. Furthermore, ΔT_l is modified by randomly appearing defects, which is unfortunate for the simulations of small and medium aspect ratios. For these reasons we prefer ΔT_{cd}. Consequently, we define the supercriticality ε as

$$\varepsilon = \frac{\Delta T_{cd} - \Delta T_c}{\Delta T_c}. \tag{2.16}$$

The temperature difference ΔT_c required for the onset of convection is the same in both scales. The Nusselt number is the ratio of the total heat flux q to that transported by conduction. It again requires the specification of which temperature difference the conductive heat flux refers to. We employ ΔT_l, i.e. we define

$$Nu = \frac{q/A}{(\lambda_l/d_l)\Delta T_l}. \tag{2.17}$$

This definition is free of the unphysical upper boundary which exists for the alternative definition

$$Nu^* = \frac{q/A}{(\lambda_l/d_l)\Delta T_{cd}} \tag{2.18}$$

frequently used in the numerical literature. To demonstrate this we assume for simplicity that the heat flux in the gas is purely conductive. The total heat flux q going through the two-layer system is then given by $q = \lambda_g A(\Delta T - \Delta T_l)/d_g$. Inserting q into (2.18) yields with use of (2.13) $Nu^* = (1+Bi)(1-\Delta T_l/\Delta T)$. Thus, $Nu^* < 1+Bi$ (Boeck & Thess 1997). However, to allow the comparison of our results with other works we translate them in parallel into Nu^* if required.

3. Methods

3.1. *The experiment*

3.1.1. *Set-up and parameters*

A sketch of the apparatus is shown in figure 2(*a*). The liquid bottom consists of a polished silicon crystal wafer which is 12.5 cm in diameter and 0.63 mm thick. This wafer is inserted up to a depth of 0.7 mm into a 5 cm thick copper block with a diameter of 17.5 cm. A 2 cm thick aluminium disk of the same diameter is pressed from below against the copper block. The disk contains, in narrow windings, 4.0 m of a thermocoax cable (Philips). To minimize lateral heat losses the copper block is placed in a vacuum. Furthermore, the outer parts of the chamber are furnished with an additional thermal insulation. The liquid layer is confined by an inner Plexiglas ring (figure 2*b*). The meniscus at this ring is avoided by filling it to its total height. The space between the inner and the outer Plexiglas ring contains the same liquid to minimize lateral temperature gradients. Before filling, the apparatus is carefully levelled. The liquid is a 10cS silicone oil (NM 10, Hüls AG) with $Pr = 100$ at $T = 25$°C. Its parameters are summarized in table 1. The liquid layer is closed from

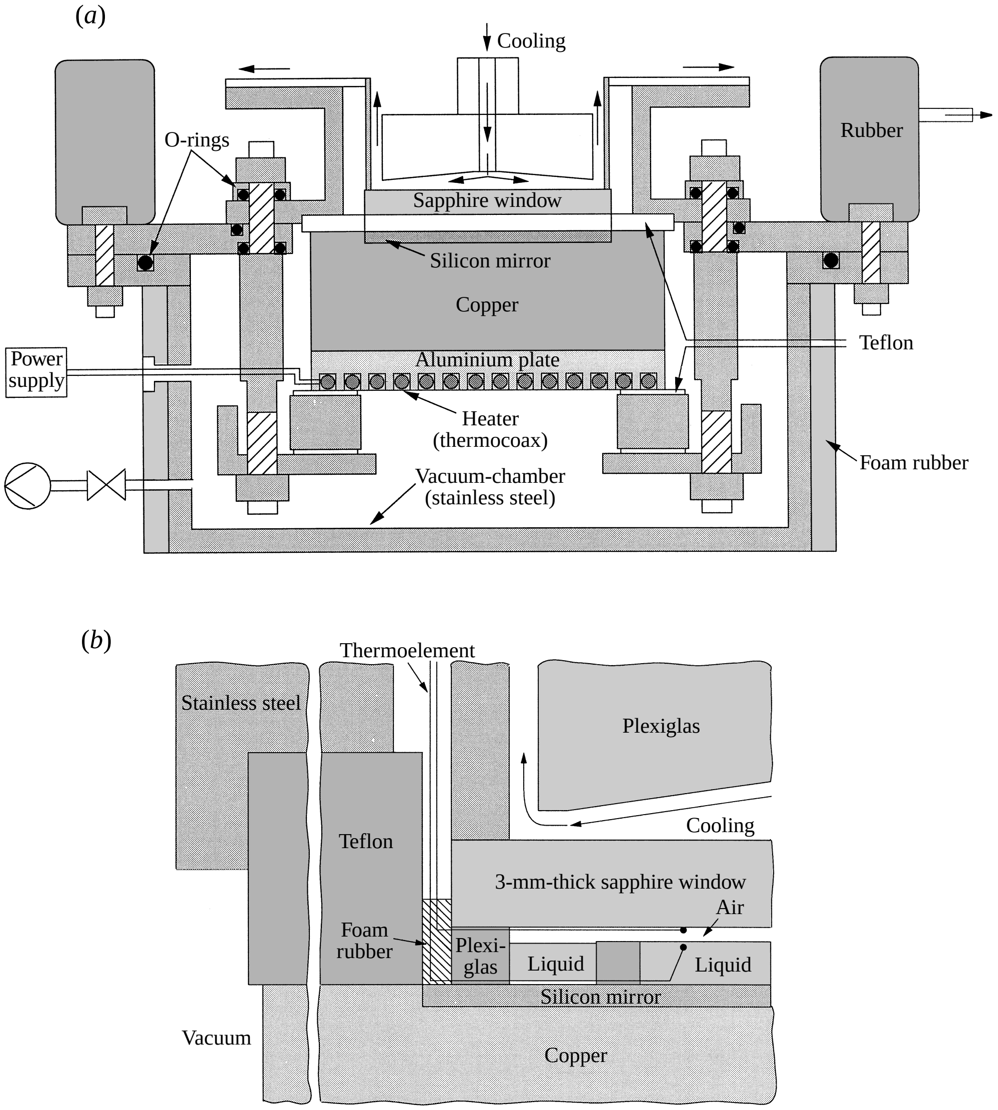

FIGURE 2. Cross-section of the experimental apparatus, shown to scale. (*a*) The complete experimental container (axisymmetric). (*b*) Embedding of the liquid and air layers in the container. Lateral close-up of the liquid layer, location of the Plexiglas rings and lead-in of the thermoelement. The vertical size of the sapphire window, silicon wafer and liquid and gas layers is enlarged by a factor of 4 in both figures, to indicate their position inside the container.

above by a transparent sapphire disc, 12.0 cm in diameter and 0.30 cm thick, placed on the outer Plexiglas ring. Sapphire is used because of its high thermal conductivity. The air layer, formed by the difference in height between the inner and outer ring, has a thickness $0.30\text{ mm} \leqslant d_g \leqslant 0.55\text{ mm}$. Since both the sapphire disc and silicon wafer are levelled to 8 in 10^5, the inhomogeneity in d_g is smaller than 15 μm. This value may be partly exceeded in the immediate vicinity of the wall due to non-homogeneous pinning of the meniscus (cf. §6). Geometric and material parameters of the air gap and the sapphire disc are given in table 1.

Quantity	Symbol	Value at 25°C
Temperature coefficient of surface tension	γ	$5.9 \times 10^{-5}\,\mathrm{N\,m^{-1}\,K^{-1}}$
Liquid kinematic viscosity	ν	$0.10 \times 10^{-4}\,\mathrm{m^2\,s^{-1}}$
Liquid density	ρ	$940.0\,\mathrm{kg\,m^{-3}}$
Liquid thermal diffusivity	κ	$0.00103 \times 10^{-4}\,\mathrm{m^2\,s^{-1}}$
Liquid thermal expansion	α	$0.0011\,\mathrm{K^{-1}}$
Liquid thermal conductivity	λ_l	$0.134\,\mathrm{W\,m^{-1}\,K^{-1}}$
Gas thermal conductivity	λ_g	$0.0261\,\mathrm{W\,m^{-1}\,K^{-1}}$ (air)
Sapphire thermal conductivity	λ_s	$41.9\,\mathrm{W\,m^{-1}\,K^{-1}}$
Liquid layer thickness	d_l	$(1.40\text{–}1.45) \times 10^{-3}\,\mathrm{m}$
Gas layer thickness	d_g	$(0.30\text{–}0.55) \times 10^{-3}\,\mathrm{m}$
Sapphire disc thickness	d_s	$2.99 \times 10^{-3}\,\mathrm{m}$

TABLE 1. Fluid and material parameter values

In contrast to the simulation where there is no buoyancy, the experiments take place at non-vanishing Rayleigh number $R = \alpha g \Delta T_{cd} d_l^3/\nu\kappa$. To quantify the ratio between both the driving forces of convection we introduce the parameter $\phi = M/R = \gamma/(\rho\alpha g d_l^2)$ where M denotes the liquid Marangoni number (3.16). Thus, for a given value d_l, ϕ remains constant independent of $T_b - T_t$. The liquid layer thicknesses used yield $\phi \approx 3$ which guarantees the dominance of surface tension over buoyancy forces. The radius r of the inner Plexiglas ring containing the liquid layer varies between 40.4 and 45.2 mm. The aspect ratio $\Gamma = 2r/d_l$ is thus $56 \leqslant \Gamma \leqslant 64$. The horizontal relaxation time $\tau_h = r^2/\kappa$ amounts to approximately 5 hours. The Biot number Bi (cf. equation (2.15)), governing that part of the temperature difference $T_b - T_w$ which occurs across the liquid layer, is $0.5 \leqslant Bi \leqslant 1.0$.

By means of a special cooling device (Koschmieder & Pallas 1974) water of temperature 18.0°C is supplied to the centre of the sapphire-disc, from where it flows radially outwards, thereby ensuring axisymmetric cooling. The cooling water, pumped with a flow rate of $95\ \mathrm{l\,h^{-1}}$, is provided from a $0.2\ \mathrm{m^3}$ thermally insulated tank. To dampen out fluctuations, its temperature is regulated by a heat exchanger. This heat exchanger is fed by a refrigerating thermostat with a temperature stability of ± 0.01 K. The temperatures of the silicon crystal, sapphire window and the cooling water at the inlet and outlet, respectively, are measured with encapsulated quartz crystals. They have a diameter of 1.8 mm and have a highly linear dependence of the resonance frequency on temperature. Temperature differences inside the liquid layer are measured with thermoelements (see §3.1.2). The temperature of the liquid bottom T_b is controlled with a regulating loop ($\pm 0.005\,\mathrm{K}$) and increased automatically in a quasi-stationary manner at a rate of $0.08\,\mathrm{K\,h^{-1}}$. The effective rate of increase of ΔT_{cd} is, according to equation (2.13), once more, smaller by the factor $Bi/(1 + Bi)$ which varies between 2 and 3. The typical duration of an experimental run, till $\varepsilon = 8$ is reached, is of the order of 350 h. Before visualization of the pattern, requiring a quick removal of the cooling device, the temperature of the liquid bottom is kept constant for one horizontal relaxation time τ_h. In table 2 we list all physical quantities which are directly accessible to measurement.

We finish this section with a general remark on the present Bénard system. On the one hand, it offers the advantage that the probability of surface contamination, from the adjacent air layer is low, due to the low surface tension of the oil used and the

Quantity	Description
T_b	Temperature at the liquid bottom
T_w	Temperature at the top of the sapphire disc
T_{in}	Temperature of the cooling water at inlet
T_{out}	Temperature of the cooling water at outlet
ΔT_{TE}	Temperature differences in the fluid layers
U	Voltage drop over the thermocoax cable
I	Current intensity
$\dot{V}$	Flow rate of the cooling water
$G(x, y)$	Shadowgraph-intensity distribution

TABLE 2. Quantities directly measurable in the experiment

small volume of the air gap. Under certain preconditions, justified by the theory and explained below, the system can be assumed to be a one-layer system and can thus be considered as the simplest system for studying STDBC. On the other hand, the range of supercriticality accessible in this system is far below that range manageable at present in RBC. This is due to the fact that the requirement for dominance of surface tension over buoyancy, expressed by the relation $\phi > 1$, demands a small liquid thickness. The critical temperature difference across the liquid layer ΔT_c, necessary for onset of convection, is proportional to the ratio between the Marangoni number and the liquid layer thickness d_l. Small values of d_l cause higher ΔT_c. We cannot reduce the thickness of the air gap below 0.25 mm, because this would cause a spontaneous wetting of the sapphire by the liquid at higher temperature gradients. Consequently, a significant part of the available temperature difference $T_b - T_w$ is lost due to the poor heat conductivity of the air gap. There is also a maximum $T_b - T_w$, up to which controlled experiments can be performed. This limitation is set by the small, but non-zero, volatility of the oil used.

3.1.2. *Temperature measurements and Nusselt number determination*

To describe our experiment in terms of the non-dimensional quantities ε and Nu we have to determine ΔT_{cd}, q and ΔT_l from the primary variables, listed in table 2. The measured temperature difference $T_b - T_w$ across the system is composed of the temperature differences across the particular layers

$$T_b - T_w = \Delta T_l + \Delta T_g + \Delta T_s, \tag{3.1}$$

as defined in figure 1. The indices l, g and s stand for liquid, gas and sapphire layer. We recall that the control parameter of the problem is (cf. §2)

$$\Delta T = \Delta T_l + \Delta T_g. \tag{3.2}$$

This quantity can precisely be determined from the experiment by using the measured heat flux q. From the continuity of the heat fluxes it follows that

$$q = q_l = q_g = q_s \tag{3.3}$$

where

$$\frac{q_s}{A} = \frac{\lambda_s}{d_s} \Delta T_s. \tag{3.4}$$

A stands for the area of the liquid layer. Using (3.1)–(3.4) we find that

$$\Delta T = T_b - T_w - \frac{d_s}{\lambda_s}\frac{q}{A}. \tag{3.5}$$

The conductive temperature drop ΔT_{cd} is then obtained from equations (3.1)–(3.5) under the assumption of purely conductive heat fluxes as

$$\Delta T_{cd} = \frac{Bi}{1 + Bi + (\lambda_g/d_g)(d_s/\lambda_s)}\ (T_b - T_w). \tag{3.6}$$

We define the temperature difference ΔT_l via

$$\Delta T_l = \Delta T - \frac{d_g}{\lambda_g}\frac{q}{A} = T_b - T_w - \left(\frac{d_s}{\lambda_s} + \frac{d_g}{\lambda_g}\right)\frac{q}{A}. \tag{3.7}$$

Let us address the question of the usefulness of definition (3.7). We consider

$$\frac{q_g}{A} = \langle \rho_g c_{p,g} v_g^{(z)} T_g \rangle + \frac{\lambda_g}{d_g}\Delta T_g \tag{3.8}$$

as an approximate representation of the heat flux in the gas gap, where c_p stands for the heat capacity. Using equations (3.2), (3.7) and (3.8) we find for the actual temperature difference ΔT_l^* across the liquid

$$\Delta T_l^* = \Delta T_l + \frac{d_g}{\lambda_g}\langle \rho_g c_{p,g} v_g^{(z)} T_g \rangle.$$

This means that our auxiliary variable ΔT_l is equal to ΔT_l^* provided that the convection in the air gap is negligible. The gas-gap convection is studied numerically in §3.2.2 and analytically in Eckert (1997). Both approaches show that air convection plays a marginal role in our parameter range. Thus, ΔT_l is nearly equal to ΔT_l^*. The Biot number modelling the heat transfer at the free surface is identical to equation (2.15) under these conditions.

The heat flux q is determined from the electric power P dissipated by the heater (figure 2*a*). P is given by the voltage drop U over the resistor R_h of the thermocoax cable and the current intensity I in the heater circuit. The power input P to the heater is divided into a part flowing through the liquid layer and a second part flowing through the insulated sidewalls, through the buffer liquid between the Plexiglas rings and through the Plexiglas rings themselves. In the purely conductive state of the liquid layer we find

$$P = \frac{\lambda_l}{d_l} A\ \Delta T_{cd} + c\ (T_b - T_w). \tag{3.9}$$

The quantity c comprises the effective thermal conductance of the sidewalls and the outer liquid and rings, respectively, and is determined from P and $T_b - T_w$, in the steady state, via a linear least-squares fit from equation (3.9) in each measurement. If c is known the heat flux q is given by $q = P - c\ (T_b - T_w)$. A question is in order regarding the constancy of c at the higher heat fluxes in the convective regime. The only heat transfer process subsumed under c which deviates slightly from linearity is the weak convection of the buffer liquid. The gap thickness between the rings is kept sufficiently small to suppress additional pattern formation. The absence of polygonal cells was verified in parallel by visualizing the pattern. The main source of the convection in the buffer liquid are small differences in surface tension due to a lateral temperature gradient. Measurements of this gradient by thermocouples show that the heat flux carried by this convection is at maximum 2% of the heat flux transported by the layer under study.

We briefly discuss the errors in the determination of ε and Nu. $T_b - T_w$ and A can be determined with an uncertainty lower than ± 0.04 K and 0.1%. According to (2.16) and (3.6) $(\varepsilon - 1)$ equals the ratio of $(T_b - T_w)$ to that at onset of convection $(T_b - T_w)_c$. $(T_b - T_w)_c$ is obtained from the Schmidt–Milverton plot (q vs. $T_b - T_w$) with an accuracy of 3%. The total error in ε amounts to 4%. The accuracy of the heat conductivities is about 1%. The error with the highest weight results from the uncertainty in the measurement of the thickness of the air gap d_g. It is determined as the difference between the heights of the outer Plexiglas ring and the liquid layer, which are both measured with a micrometer screw (uncertainty ± 0.01 mm). Depending on the thickness of the air gap, the relative error lies between 2% and 3.3%. The heat flux q is systematically overestimated on average by 1% due to neglecting to measure the weak convection in the buffer liquid. The total error in q amounts to 3–4%. According to equations (3.6) and (3.7) the average errors in ΔT_{cd} and ΔT_l are then 5% and 12%, respectively. Consequently, the cumulative error in Nu is on average 17%.

To measure local temperature differences single thermoelements are inserted into the liquid layer. For one thermoelement we use two pairs of 0.08 mm copper and constantan wires. Via a special welding technique we produce very fine welding points with sizes of the order of the thickness of the wire. One of these welding points is placed either onto the silicon wafer or onto the sapphire window (figure 2*b*). The other one is inserted from the bottom and positioned at least 0.05 mm below the liquid surface. The liquid surface is kept free of disturbances. The height of the upper welding point is determined with a micrometer screw. The thermoelements are connected to a 6.5-digit voltmeter.

3.1.3. *Pattern visualization and Fourier-space-representation*

For the visualization of the convective pattern we use a standard shadowgraph technique (Merzkirch 1974). A point-like light source, produced by a projector including a heat filter, is projected onto an achromat of 15 cm in diameter. The beams are made parallel and turned by a large beam splitter, in order that they fall onto the liquid layer at an angle of 90° relative to the liquid bottom. The beams are reflected at the polished silicon wafer, and pass again through the beam splitter to produce a two-dimensional grey value distribution $G(x, y)$ on a screen. Here it is photographed by a CCD camera switched to a frame grabber card (Matrox, $768 \times 512 \times 8$ bit).

For the presentation of the results it is useful to switch between shadowgraph images in physical space and their representation in Fourier space. From the digitized grey value distribution we calculate via two-dimensional-Fourier transformation the power spectral density $P(k, \varphi)$, where k and φ denote the polar coordinates in the two-dimensional wavenumber space. An appropriate tool for characterizing changes in the orientation of cell domains is the azimuthal distribution function $Q(\varphi)$. Following Gollub & McCarriar (1982) we define

$$Q(\varphi) = \frac{1}{W} \int_{\langle k \rangle - \Delta k}^{\langle k \rangle + \Delta k} k P(k, \varphi)\, \mathrm{d}k, \qquad (3.10)$$

where W is a normalization factor. The domain of radial integration is restricted to an interval $[\langle k \rangle - \Delta k, \langle k \rangle + \Delta k]$, where $\langle k \rangle$ is the average wavenumber and $\Delta k = 0.15 \langle k \rangle$.

We introduce $\langle k \rangle$ as

$$\langle k \rangle = \int_0^\infty \int_0^{2\pi} k^2 P(k,\varphi)\,\mathrm{d}k\mathrm{d}\varphi \bigg/ \int_0^\infty \int_0^{2\pi} k P(k,\varphi)\,\mathrm{d}k\mathrm{d}\varphi. \tag{3.11}$$

Before starting the integration of equations (3.10) and (3.11), several preprocessing steps are undertaken. As shown later, STDBC becomes increasingly complex with increasing ε since cells of different planform appear which still partly deviate from the equilateral form. To determine $Q(\varphi)$ and $\langle k \rangle$ of cells of a given planform we use special graphics software by which we separate domains of different symmetries. We do this by cutting domains of equal planform with a rectangular window. The isolated cell domains are multiplied by a Parzen window and brought together as a new picture, which contains only islands of cells with equal symmetry. In the hexagonal regime of convection the window lies entirely in the box; by this we exclude the sightly larger, incomplete rim cells. Finally, this new, separated picture serves as input quantity for equations (3.10) and (3.11). Both integrals are computed using bicubic spline interpolation. Higher harmonics are filtered out by a binomial filter.

3.2. *Numerical simulation*

3.2.1. *Outline of the numerical strategy*

In principle, there is no conceptual or technical difficulty in performing a direct numerical simulation of the two-layer equations (2.2)–(2.4) by extending previous numerical work for the one-layer equations (Bestehorn 1993, 1996; Thess & Orszag 1995). However, it turns out that such an approach is not necessary in the parameter range covered by our experiment. More precisely, we have performed a two-dimensional reference simulation of the full two-layer equations (2.2)–(2.4), demonstrating that the convection of the air layer has little bearing on the motion of the silicone oil. Below we shall show how the results of the reference simulation can be used to convert the two-layer problem into a one-layer problem with an effective Biot number that can be evaluated systematically.

3.2.2. *Reference simulation of the two-layer equations in two dimensions*

To study the influence of the motion of the air layer we first solve the complete set of equations (2.2)–(2.4) in two spatial dimensions. For the numerical integration we apply a simple explicit Euler method. The solutions converge rather fast to stationary patterns after about one vertical heat diffusion time in the range up to $M_{tot} = 1000$. In the lateral direction we use periodic boundary conditions. The lateral dimension was chosen in such a way that a pair of rolls with wavenumber $k = 2$ fits in. We insert the parameters $Pr_g = 0.6$, $Pr_l = 100.0$, $\kappa_g/\kappa_l = 270.0$, $\lambda_g/\lambda_l = 0.19$, $d_g/d_l = 1/3$, valid for 10 cS silicone oil and air at room temperature, to allow direct comparison with the experiment. Figure 3 shows the contour lines of the stream function and the temperature field at two different values of M_{tot}. We find that the isotherms in the air layer are nearly non-deformed, i.e. only weakly influenced by the convection. To evaluate quantitatively the importance of convective heat transfer we determine numerically the Nusselt numbers

$$Nu_l = \frac{\langle \partial_z T_l \rangle}{\langle T_s \rangle - T_b}, \qquad Nu_g = \frac{\langle \partial_z T_g \rangle}{T_t - \langle T_s \rangle}$$

of the liquid and gas, respectively. Here $\langle\cdot\rangle = (1/L)\int_0^L \mathrm{d}x\ \cdot$ is the average over the periodicity length L evaluated at the free surface and $\langle T_s \rangle$ is the mean surface

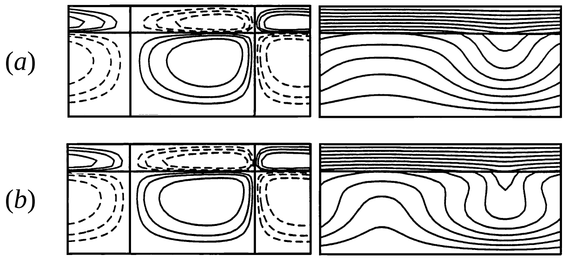

Figure 3. Numerical solutions of the full two-layer system in two spatial dimensions: (*a*) $\varepsilon = 0.7$ and (*b*) $\varepsilon = 3.0$. Left: Stream function, solid lines denote vortices turning clockwise, dotted counter-clockwise. The motion in the air layer is induced by the boundary condition at the interface. Right: isotherms. In the air gap, the isotherms are nearly parallel and therefore virtually not influenced by convection, even at moderate ε.

M_{tot}	Nu_l	Nu_g	Figure
360	1.170	1.000	3(*a*)
850	1.623	1.000	3(*b*)

Table 3. Two-dimensional simulation of the two-layer Bénard system: Nusselt numbers for the liquid and the gas layers at different M_{tot}. Note that the Nusselt number of the air is not affected by the convection in the liquid layer.

temperature. Table 3 summarizes the values of Nu_l and Nu_g for two different values of the total Marangoni number. The main result is that the Nusselt number of the air layer is nearly independent of the convection in the liquid layer. We find deviations from the conductive state of the air which are less than 0.01% for $M_{tot} \leqslant 1000$. This is below our numerical accuracy. Thus, our reference simulation demonstrates that the assumption of a static air layer is a very good approximation in the parameter range of the experiment.

3.2.3. *Formulation of the effective one-layer equations in three dimensions*

As demonstrated above, STDBC can be described in the parameter range of the experiment by the motion of the liquid alone. The air is considered at rest and the thermal properties of the air layer are contained in an extra boundary condition for the temperature at the free surface of the liquid. A reference value is the temperature T_I of the free surface without convection. Using equation (2.13) T_I is given by

$$T_I = T_b - \Delta T_{cd} = T_b - \frac{1}{1 + \lambda_l d_g / \lambda_g d_l} (T_b - T_t). \tag{3.12}$$

The temperature and length are now scaled by $T_i = T_i'/(T_b' - T_I')$ and $z = z'/d_l$, respectively, where the prime refers to the variable in physical units. Separation of the linear profile introduces the new variable Θ:

$$T_l = T_b - (T_b - T_I)z + \Theta(x, y, z, t). \tag{3.13}$$

The boundary condition on the bottom (2.5) immediately yields

$$\Theta = 0 \qquad \text{for } z = 0. \tag{3.14}$$

At the free surface, the second terms on the right-hand sides of (2.9) can be neglected since $\rho_l \nu_l \gg \rho_g \nu_g$ for an oil/air system. Using (2.3) we get

$$\partial_z^2 v_l^{(z)} = M(\partial_x^2 + \partial_y^2)\Theta \qquad \text{for } z = 1 \tag{3.15}$$

with the dimensionless parameter

$$M = \frac{\gamma(T_b' - T_l')d_l}{\rho_l \nu_l \kappa_l} \tag{3.16}$$

usually denoted as the Marangoni number, related to M_{tot} by

$$M = M_{tot}\frac{\lambda_g}{\lambda_l}\,\frac{1 + d_l/d_g}{1 + \lambda_g d_l/\lambda_l d_g}. \tag{3.17}$$

To derive the thermal boundary condition at the surface we combine (2.7)–(2.8) with (3.13) to find

$$\partial_z \Theta = \frac{\lambda_g}{\lambda_l}\partial_z T_g|_{z=1} + (T_b - T_l) \tag{3.18}$$

which involves the temperature of the gas layer. Since we need not pay attention to the convection in the gas layer, the continuity of the temperature at the interface allows us to express T_g with the value of Θ along the interface. We obtain a non-local boundary condition of the general form

$$\partial_z \Theta(x, y, z)|_{z=1} = \lambda_g/\lambda_l \int_0^{L_y}\int_0^{L_x} \mathrm{d}x'\mathrm{d}y'\, G(\boldsymbol{x} - \boldsymbol{x}')\Theta(x', y', 1) \tag{3.19}$$

with the kernel G resulting from inversion of the heat equation. Physically the non-locality comes from the coupling of the interface to the air which connects all points of the interface instantaneously via heat diffusion. To avoid non-local expressions one usually truncates the gradient expansion of (3.19) after the leading term and finds the condition

$$\partial_z \Theta = -Bi\Theta \tag{3.20}$$

with $Bi = \lambda_g d_l/\lambda_l d_g$ as the Biot number, which is a good approximation for $d_g/d_l \ll 1$. If $d_g/d_l = O(1)$, which is the case for our experiments as well as for the numerical simulations of the previous paragraph, an approximation of (3.19) leads to a relation like (3.20) with a slightly different effective Biot number, in the following denoted as Bi_{eff}.

From our reference simulation we may estimate Bi_{eff} in the following way: knowledge of the temperature at the interface allows us to match the exact condition (3.18) onto the approximation (3.20). Projecting the right-hand side of (3.18) onto Θ, we obtain

$$Bi_{eff} = -\frac{\displaystyle\int_0^L \mathrm{d}x\,(\lambda_g/\lambda_l \partial_z T_g|_{z=1} + T_b - T_l)\Theta|_{z=1}}{\displaystyle\int_0^L \mathrm{d}x\,\Theta^2|_{z=1}}. \tag{3.21}$$

Table 4 shows that Bi_{eff} decreases slightly with increasing M. This is due to the growing contribution to (3.21) from modes with zero wavenumber. Inspection of the gradient expansion of (3.19) shows that temperature distributions with larger wavenumbers contribute more strongly to an effective Biot number.

If not otherwise indicated, the effective Biot number of the simulation equals the Biot number of the experiment (cf. (2.15)). In the following numerical treatment it is

Figure	M_{tot}	ε	Bi_{eff}
3(*a*)	360	0.7	0.63
3(*b*)	850	3.0	0.60

TABLE 4. Effective Biot number as function of ε

of advantage to use the incompressibility condition (2.3). The solenoidal velocity field of the liquid can be separated into its toroidal and poloidal parts, according to

$$\boldsymbol{v}(\boldsymbol{r},t) = \nabla \times \{\phi(\boldsymbol{r},t)\boldsymbol{z}_0\} + \nabla \times \nabla \times \{\psi(\boldsymbol{r},t)\boldsymbol{z}_0\} \tag{3.22}$$

where $\boldsymbol{z}_0$ denotes the unit vector in the vertical direction. The scalar field ϕ is a stream function that describes the horizontal mean flow. Forming the curl and twice the curl of the Navier–Stokes equations we obtain

$$\left\{\Delta - \frac{1}{Pr}\partial_t\right\}\Delta\Delta_2\psi = -\frac{1}{Pr}\{\nabla \times \nabla \times (\boldsymbol{v}\cdot\nabla\boldsymbol{v})\}_z, \tag{3.23a}$$

$$\left\{\Delta - \frac{1}{Pr}\partial_t\right\}\Delta_2\phi = -\frac{1}{Pr}\{\nabla \times (\boldsymbol{v}\cdot\nabla\boldsymbol{v})\}_z, \tag{3.23b}$$

and from (2.4)

$$\{\Delta - \partial_t\}\Theta = \Delta_2\psi + \boldsymbol{v}\cdot\nabla\Theta. \tag{3.24}$$

Here we suppressed the suffix i since all quantities refer to the liquid layer. From (3.23*b*) it is obvious that the mean flow generation is proportional to $1/Pr$ and that the mean flow vanishes for an infinite Prandtl number.

For the boundary conditions on the bottom, $z = 0$, we have

$$\Theta = \phi = \psi = \partial_z\psi = 0. \tag{3.25}$$

On the top ($z = 1$) we find that

$$\psi = 0, \quad \partial_z\phi = 0, \quad \partial_z^2\psi = -M\Theta, \quad \partial_z\Theta = -Bi_{eff}\Theta \tag{3.26}$$

To solve the fully nonlinear problem constituted by (3.23)–(3.26), we use the algorithm described in Bestehorn (1996). In the two lateral directions periodic boundary conditions are assumed. The parameter spaces accessible to experiment and simulation do not completely overlap. In comparison to other disciplines, such as turbulence research, the gap is rather small. So, the same ε-values as in the experiment can be achieved if a lower Prandtl number is used in the simulation. At even smaller Prandtl numbers (e.g. $Pr = 40$) the maximum ε-value of the simulation already exceeds that of the experiment.

4. The hexagon–square transition

4.1. *Phenomenology*

The main result of the present work is the identification of square cells as a stable mode of STDBC, both in experiment and numerical simulation. A first glimpse of the pattern formed in experiment and simulation is given in figure 4 which is the shadowgraph intensity distribution in part of the experimental box at $\varepsilon = 7.0$ ($Pr = 100$) together with the surface temperature field as obtained from numerical simulations at $\varepsilon = 3.0$ ($Pr = 50$). The figure reflects the robustness of the phenomenon and the distinct

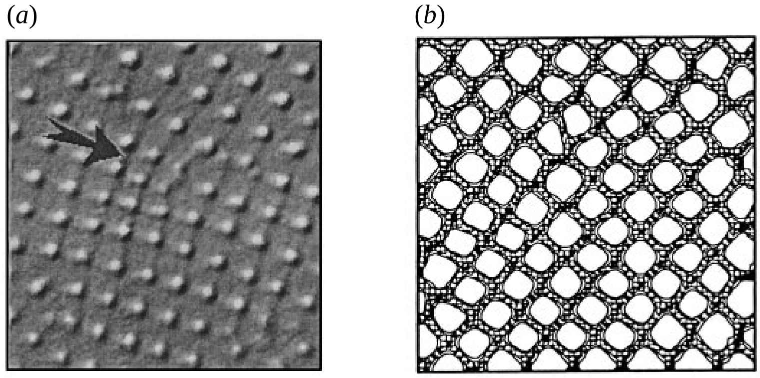

FIGURE 4. Robustness of square cells in Bénard convection: (*a*) experiment ($\varepsilon = 7.0$, $Pr = 100$, $\Gamma = 64$), (*b*) numerical simulation ($\varepsilon = 3.0$, $Pr = 50$, $\Gamma = 32$). The high structural similarity of both patterns includes the defect type: a dislocation is present in both pictures, and located at nearly the same place (see arrow in *a*). The shadowgraph image in (*a*) is treated with a nonlinear pseudo-filter; (*b*) shows the isotherms at the surface.

structural similarity in the pattern formation in experiment and simulation. The latter manifests itself also in the presence of the same type of defect, namely a dislocation in a square lattice indicated in figure 4(*a*). Square patterns appear in both experiments and simulations as an intrinsic, i.e. stable and reproducible, planform of STDBC, if ε is increased beyond a certain threshold ε_s. With lowering of ε below $\varepsilon_s^{sub} < \varepsilon_s$ they disappear. The values of ε_s and ε_s^{sub}, detailed below, differ, which is due to the presence of a hysteresis (cf. §5.3).

Figure 5, in which we plot shadowgraph intensity fields together with the corresponding orientational distribution functions in Fourier space, summarizes the most important features of the nonlinear evolution of hexagonal cells towards square cells. Starting at $T_b - T_w = 0$ we increase the temperature difference across the system in a quasi-stationary manner. With the onset of the primary instability ($\varepsilon = 0$), the liquid layer is tessellated by well-ordered hexagonal cells. The hexagonal pattern can be preserved up to $\varepsilon \sim 3.2$ if the noise level is sufficiently low. Figure 5(*a*) displays an example for $\varepsilon = 2.4$. It shows two large regions of hexagons having a slightly different orientation. They are linked by four pentagon-heptagon defects, lined up in the centre of the container. Looking at the orientational distribution function $Q(\varphi)$, we observe six peaks that are typical of the hexagonal symmetry. They are partly widened due to the weak orientational non-uniformity introduced by the defects.

At a certain ε (see §4.2) the number of 'free' pentagons which are not bounded in a pentagon-heptagon defect starts to increase. The pentagon of this defect seems to act as a nucleus for the generation of the 'free' pentagons. Typically, these pentagons are organized in 'double' lines, which we henceforth call 'penta-lines'. We illustrate this step in figure 6(*a*). The relevance of these aggregates is also supported by numerical simulation (see e.g. figure 17*b* in §5.3). The place of their generation seems to be chosen at random. Medium aspect ratios favour places in the vicinity of the rim. From there the penta-lines are directed radially inwards towards the centre of the box. At larger aspect ratios the penta-lines are also generated in the central parts of the container. The mechanism leading to the formation of these kind of pentagons seems to be generic. It triggers the entire transformation process from hexagons to squares. Two adjacent cell knots of a hexagonal cell move towards each other along one of the three lines of symmetry. They merge and one cell edge vanishes. The

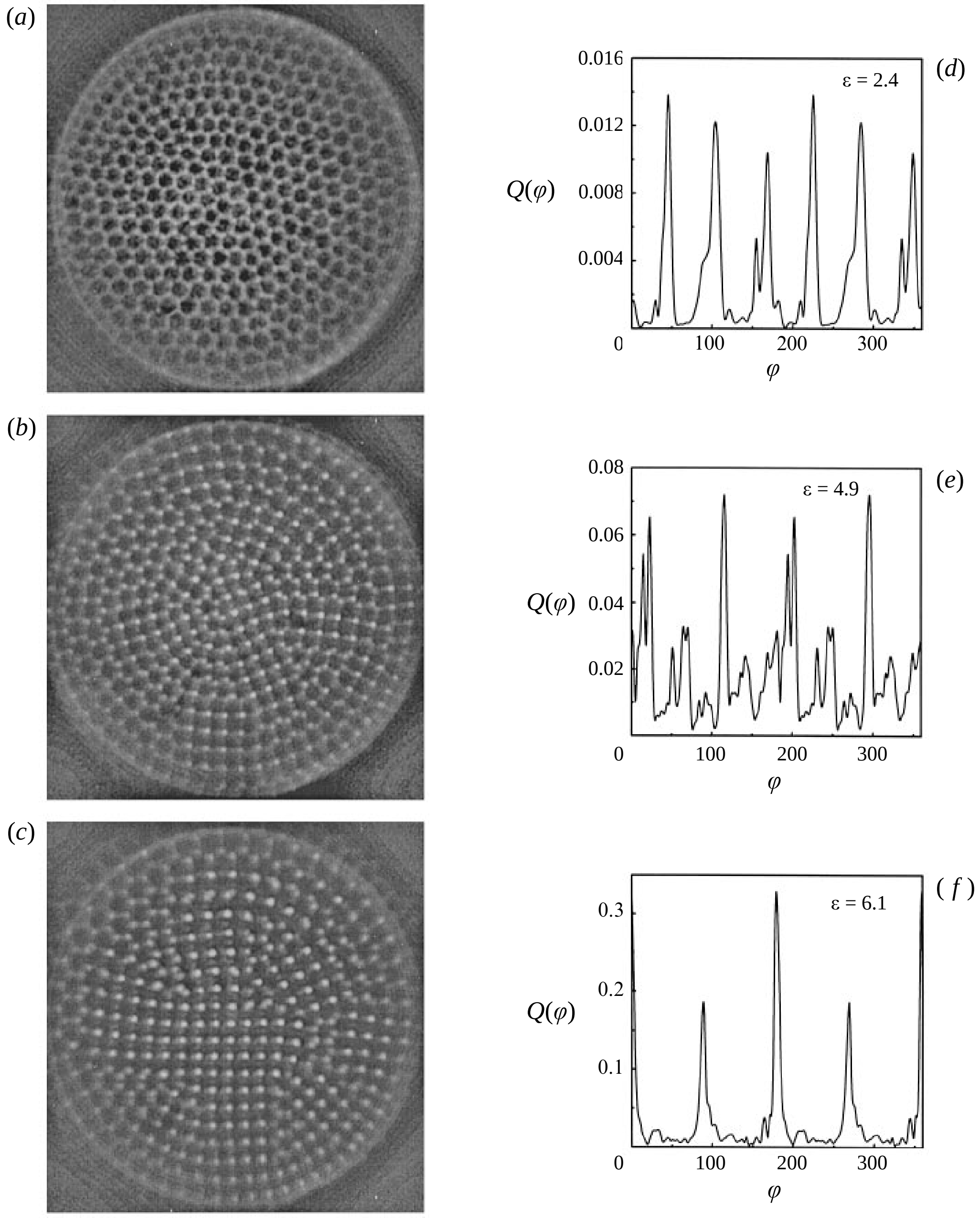

FIGURE 5. The hexagon–square transition in STDBC in the experiment. Shadowgraph pictures at $\varepsilon = 2.4$ (*a*), $\varepsilon = 4.9$ (*b*) and $\varepsilon = 6.1$ (*c*) together with the corresponding orientational distribution functions (*d–f*). ($d_l = 1.41$ mm, $d_g = 0.26$ mm, $\Gamma = 64$, $Pr = 100$).

pentagons so formed are, as a rule, non-equilateral, and orientated with the shortest edge towards remaining hexagonal cells (cf. figure 6*a*). On increasing ε, these sides become shorter and shorter. Consequently, square cells are formed in the interior of such a penta-line. The two fronts of pentagons tend to spread into hexagonal domains. This step is sketched in figure 6(*b*).

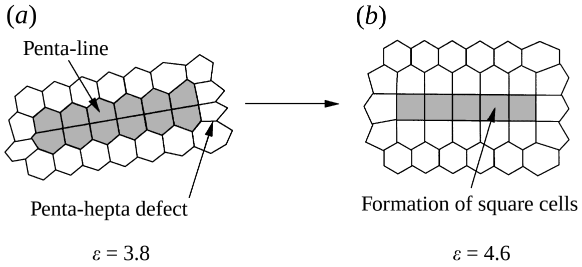

FIGURE 6. Transformation process from hexagons to squares in the experiment. (*a*) Formation of a double line of pentagons ('penta-line') which has its origin at the pentagon of the penta-hepta defect. (*b*) Undoing of the penta-line and spreading of two fronts of pentagons into hexagonal areas. In the interior of the original penta-line square cells are formed.

We return to the description of the transition. Figure 5(*b*) displays an intermediate stage of the pattern in its evolution to a square planform. The process sketched above can occur with different degrees of perfection. Islands of square cells are distributed between hexagonal domains and separated by fronts of pentagons. The respective spectrum (figure 5*e*) is more irregular due to splitting of peaks. The reason is the partial alignment of square cells along one of the lines of symmetry of the former or the still existing hexagonal domains.

The shadowgraph picture of the final stage is shown in figure 5(*c*). It is characterized by square cells concentrated in domains of different extension and orientation. Our experiment demonstrates that for sufficiently large ε the competition between hexagons and squares is resolved in favour of the latter (cf. figure 5*f*). However, the hexagons are not completely expelled by square domains but, to a small extent, persist with a remarkable degree of stability. This fact is both a consequence of the circular geometry and of the rather high Prandtl number as discussed in §4.4. The existence of a perfectly square pattern in the numerical simulation for a periodic square domain leaves little doubt that an experiment in a square box with a liquid of $Pr \sim 50$ or lower would provide a pattern of square domains without intermediate hexagons.

4.2. *Composition of the convective pattern*

To quantify the composition of the pattern as a function of ε we introduce relative cell numbers $p_i = N_i/N$, defined as the ratio between the number of cells N_i of a given planform (hexagons ($i = 6$), pentagons ($i = 5$), squares ($i = 4$)) and the number of complete cells N. We exclude cells which are situated along the perimeter of the container. The behaviour of p_i at $Pr = 100$ with an aspect ratio $\Gamma = 64$ is shown in figure 7.

At the onset of convection the pattern comprises approximately 350 cells which are almost completely hexagonal, i.e. $p_6 = 0.98$. The deviation of p_6 from unity is due to a small number of heptagonal and pentagonal cells, which are unified in penta-hepta defects. With increasing ε we do not find a monotonic increase of this kind of defect. Up to $\varepsilon \sim 1$ the hexagon percentage p_6 can be kept as high as $p_6 = 0.96 \pm 0.03$ (figure 7*a*). The fluctuation is due to spontaneous generation and annihilation of penta-hepta defects. Beyond $\varepsilon \sim 2$, p_6 starts to decrease slowly at the expense of a growing pentagon number p_5 (figure 7*b*). These pentagons are no longer completely linked to heptagons but become more and more organized in the penta-lines already described in §4.1. Beyond $\varepsilon = 4$, p_6 decreases drastically. In parallel, we detect a significant increase in p_4. The pentagon number p_5 grows, too, but at a slower rate,

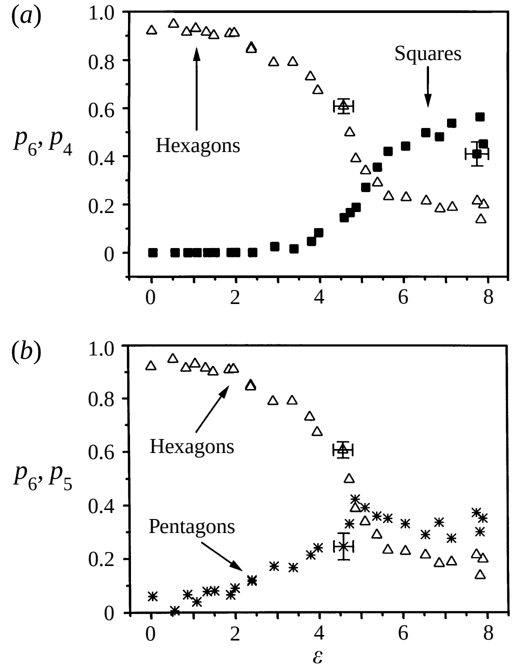

FIGURE 7. Composition of the Bénard pattern. Fraction of a cell class p_i as a function of ε. $i = 4, 5, 6$ stands for square, pentagonal and hexagonal cells. ($d_l = 1.41$ mm, $d_g = 0.26$ mm, $\Gamma = 64$, $Pr = 100$).

and reaches a maximum at $\varepsilon \sim 4.7$. Above this value, it again decreases slowly. At $\varepsilon \geqslant 6.5$ the p_i-values show minor changes only. An increase of p_4 above 55% was not observed for the aspect ratio under study ($\Gamma = 64$).

In spite of many similarities, this result deviates from observation for medium aspect ratios ($\Gamma = 46$) (Nitschke-Eckert & Thess 1995), where $p_4 = 0.70$ could be realized. The role of pentagons as mediating aggregates of the transition is identical for all aspect ratios studied. The maximum in the p_5-distribution, however, is more pronounced for the medium than for the large aspect ratio.

From figure 7(*a*) one can derive a threshold ε_s^p for the onset of convection in square cells. The superscript p indicates that this value originates from the p_4-distribution. We define ε_s^p as the point at which the p_4-distribution starts to grow systematically. It is calculated as the intersection between a linear least-squares fit, containing the data up to $p_4 = 0.3$, and the abscissa. Taking into account all experimental runs for $\Gamma = 64$, we find that

$$\varepsilon_s^p = 4.0 \pm 0.5. \tag{4.1}$$

The error $\Delta\varepsilon = \pm 0.5$ includes the standard deviation and the scatter between independent experimental runs. The measure ε_s^p is afflicted with the ambiguity in the choice of the range and the type of the fit. This uncertainty is removed later on by introducing a second measure, based on the heat flux measurements, to be discussed in §5.1. We shall see that the value of ε_s^p is close to this second measure.

4.3. *Wavenumbers of hexagonal and square cells*

On increasing ε, Bénard convection becomes increasingly complex. First, the cellular pattern can comprise cells of different planform. Second, the cells can deviate from the equilateral form. The determination of the wavenumber of such a pattern can

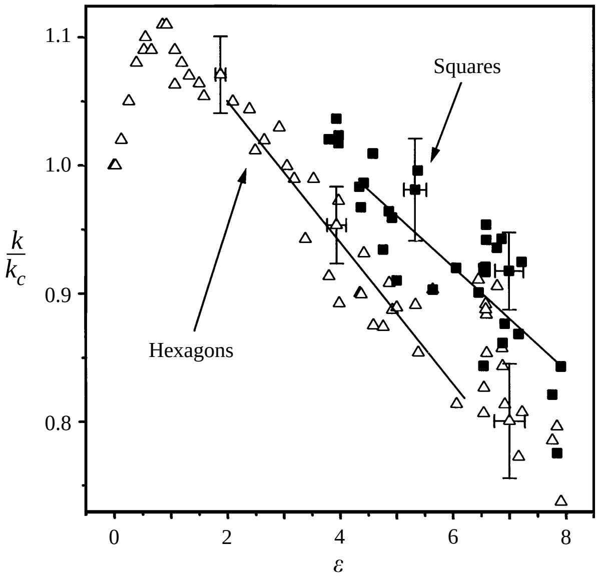

FIGURE 8. Measured wavenumbers of hexagonal and square cells as a function of ε. $k_c = 1.60\ \mathrm{mm}^{-1}$ is the wavenumber at the onset of convection. ($\Gamma = 64$, $d_l = 1.41$ mm, $d_g = 0.26$ mm, $Pr = 100$).

be done in both physical and Fourier space. Both approaches are used in this work. The k-determination based on Fourier transformation, however, is given preference because this method is easier to formalize. The procedure was described in §3.1.3 where we introduced the average wavenumber $\langle k \rangle$, cf. (3.11).

The measured dependence of the integral wavenumber $\langle k \rangle$ on ε in a container with $\Gamma = 64$ is shown in figure 8. While previous measurements of the wavenumber (Cerisier *et al.* 1987*b*; Koschmieder & Switzer 1992) were restricted exclusively to the hexagonal or the hexagonal/pentagonal cell planforms, our experiment permits us to draw a more complete picture of the wavenumber behaviour at higher values of ε. The initial increase of the wavenumber in the hexagon regime, $\mathrm{d}(\langle k \rangle / k_c)/\mathrm{d}\varepsilon = 0.18$, or in different notation $\mathrm{d}\langle k \rangle / \mathrm{d}M = 0.0036$ at $\phi = 2.9$, is in qualitative agreement with the work of Koschmieder (1991), Koschmieder & Switzer (1992), who found $\mathrm{d}k/\mathrm{d}M = 0.0042$ for $\phi = 4.2$. Beyond the k-maximum, whose value and location is a function of ϕ, the size of the cells increases monotonically with ε. This behaviour is qualitatively not changed by the appearance of the square cells. The remarkable feature, however, is the difference in the wavenumber between hexagonal and squares cells clearly visible in figure 8. On calculating the ratio $\langle k_4 \rangle / \langle k_6 \rangle$ in the range $4.5 \leqslant \varepsilon \leqslant 6.5$ for each ε, we obtain on average

$$\overline{\langle k_4 \rangle / \langle k_6 \rangle} = 1.08 \pm 0.02. \tag{4.2}$$

The ε-range was chosen in such a manner that the fractions of hexagons and squares are comparable and fulfil the condition $0.2 \leqslant p_i \leqslant 0.6$ (cf. figure 7). Our experiment demonstrates that square cells posses a wavenumber which is, on average, 8% higher than that of hexagonal cells at the same ε. The 'thermal expansion coefficient' $\mathrm{d}(\langle k \rangle / k_c)/\mathrm{d}\varepsilon$ is different for both cell types. Using linear least-squares fits we find

$$\frac{\langle k_6 \rangle}{k_c} = -0.055\ \varepsilon + 1.161 \qquad \text{for } 2.0 \leqslant \varepsilon \leqslant 6.0, \tag{4.3}$$

$$\frac{\langle k_4\rangle}{k_c} = -0.40\ \varepsilon + 1.163 \quad \text{for } 4.4 \leqslant \varepsilon \leqslant 8.0. \tag{4.4}$$

Obviously, the size of hexagons increases faster than that of square cells. The upper [lower] boundary of the fit ranges of hexagons [squares] is set by the ε-value at which the fraction p_i of the particular cell class remains less than 0.2.

The measurements of $\langle k\rangle$ based on Fourier transformation are supported by measurements in physical space. Assuming regular planforms, the wavenumber is related to the edge lengths of the hexagonal and square cells, l_6 and l_4, via

$$k_6 = 4\pi/3l_6, \tag{4.5}$$

$$k_4 = 2\pi/l_4 \tag{4.6}$$

(Chandrasekhar 1961). The physical-space equivalent to $\langle k_i\rangle (i = 4, 6)$ is the mean value $\langle l_i\rangle$ of the corresponding edge-length distribution. These quantities are obtained from a statistical analysis of the Bénard cells (Thiele & Eckert 1997). For the average edge-length ratio in the same range $4.5 \leqslant \varepsilon \leqslant 6.5$ we find $\overline{\langle l_6\rangle/\langle l_4\rangle} = 0.72 \pm 0.04$. According to equations (4.6) and (4.5) this translates into $\overline{\langle k_4\rangle/\langle k_6\rangle} = 1.08 \pm 0.05$, in agreement with the results obtained in Fourier space.

The higher wavenumber of square cells is surprising. It partly supports the maximum heat transfer hypothesis (Malkus & Veronis 1958) which implies a smaller wavelength for the selected mode of higher heat transport (Busse 1967). We now wish to study the wavenumber of the *mode with maximum heat transfer* by means of numerical simulation. For this purpose we solve (3.23) and (3.24) on a unit cell of length L_x, L_y, chosen in such a way that one regular square or hexagon fits in. The periodicity lengths L_x, L_y thereby determine the wavelength of the pattern and enter the program as a free parameter – an advantage that cannot be directly realized in the experiment. To determine the Nusselt number and the periodicity length we use the following procedure: first we fix the number of lateral mesh points at 16×16 for squares and at 32×18 for hexagons. The latter is a reasonable approximation of $\sqrt{3}/2$ which is the lateral aspect ratio of a hexagonal unit cell. Then we integrate (3.23) and (3.24), using a square or a hexagon as initial condition and a starting value Δx for the lateral step size between two mesh points. We obtain

$$L_x = L_y = 16\Delta x, \quad k_4 = \frac{\pi}{8\Delta x} \quad \text{(squares)}, \tag{4.7}$$

and

$$L_x \approx (\sqrt{3}/2)L_y = 18\Delta x, \quad k_6 = \frac{\pi}{16\Delta x} \quad \text{(hexagons)}. \tag{4.8}$$

The integration is stopped when the absolute change of the Nusselt number is less than 10^{-6}. Then we vary Δx until the maximum of the Nusselt number is reached. In that way we find k_4 and k_6 maximizing the Nusselt numbers for various values of the control parameter ε. This relation is shown in figure 9. The behaviour of the hexagon wavenumber as a function of ε coincides well with the experimental facts presented above. A rather strong increase for weakly supercritical convection is followed by a maximum at about $\varepsilon = 0.7$ and a slow decrease of the wavenumber thereafter. Note that this behaviour is obtained without any buoyancy influence. Unlike the experiment, the wavenumber k_4^{max} of the square cell which maximizes the heat transfer is lower than that of the corresponding hexagonal cell. We find that

$$k_4^{max}/k_6^{max} = 0.96 \pm 0.01 \tag{4.9}$$

which behaves nearly reciprocally to the result found in the experiment.

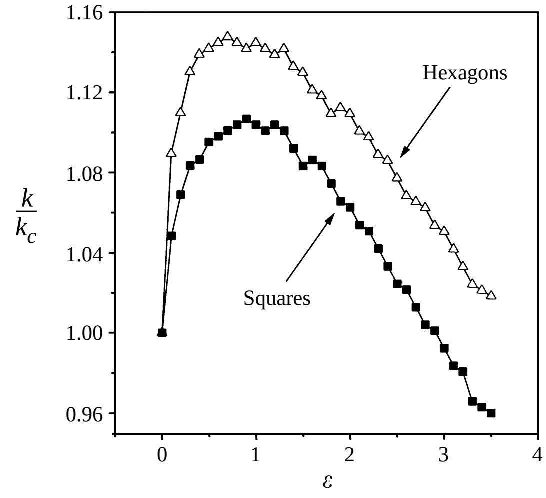

FIGURE 9. Normalized wavenumbers of the *mode of maximum heat transfer* as obtained from numerical simulations of a hexagonal and a square cell, respectively, at $\phi = 0$. The variation of the periodicity length of one elementary cell gives different values for the wavenumber k. The plot shows the k-values that maximize the Nusselt number.

4.4. *Prandtl number dependence*

The possibility of varying material parameters of the liquid over a wide range is an advantage of the numerical simulation in comparison to the experiment. To study the dependence of the transition on the Prandtl number we therefore resort to numerical results. The computations are carried out with medium-aspect-ratio layers ($L_x/d_l = L_y/d_l \approx 23$) simulated on a grid of $64 \times 64 \times 15$ points, and to obtain higher accuracy, on $96 \times 96 \times 15$ points. For all runs a random initial condition is chosen. The numerical integration is completed with a steady state when the Nusselt number reaches a constant value.

We find that the Prandtl number plays a key role in regard to the planform selection. In figure 10 we illustrate this influence by presenting three steady states obtained from the same random initial condition and the same value of ε but three different Prandtl numbers. The cells are reconstructed by means of the Wigner–Seitz construction (see textbooks of solid state physics such as Kittel 1966). For clear illustration, every planform is characterized by a separate colour. Moving in the direction towards smaller Prandtl numbers (from *a* to *c*) we observe two marked tendencies. Firstly, we find an increase of the number of square cells. This increase is, secondly, accompanied by an alignment of the squares in increasingly regular domains (cf. figures 10*a* and *c*). From this behaviour one can argue that the onset of the transition is influenced by the Prandtl number. In table 5 we demonstrate that on increasing the Prandtl number a higher ε is required to transform hexagons into squares and vice versa.

On extrapolating the values of table 5 to the Prandtl number of the experiment, using the fit $\varepsilon_s^{sim} = 0.28\ Pr^{0.68}$, we obtain $\varepsilon_s^{sim}(Pr = 100) = 6.4 \pm 0.6$. The error given is caused both by the uncertainty of ± 0.1 in the determination of ε_s^{sim} and by the non-uniqueness of the fit. The value of ε_s^{sim} will be compared to the experimental one in §5.1.

The reason for the Prandtl number influence lies in the fact that the vertical vorticity present for any finite Pr is of order $1/Pr$. This vorticity seems to act as a 'lubricant' and may help to 'soften' the structure. Pattern dynamics then may overcome the

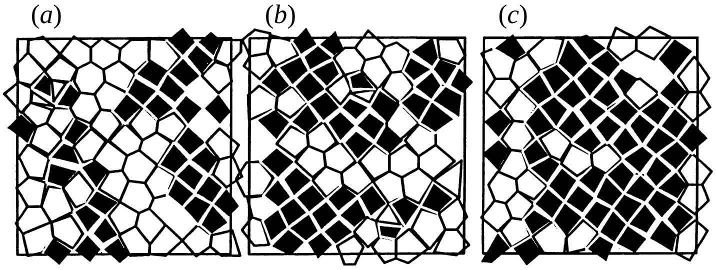

FIGURE 10. Influence of the Prandtl number on the pattern selection at $\varepsilon = 4.0$ ($Bi = 0.1$). (*a*) $Pr = 10000$: $p_4 = 0.4$, $p_5 = 0.45$, $p_6 = 0.06$; (*b*) $Pr = 500$: $p_4 = 0.45$, $p_5 = 0.4$, $p_6 = 0.05$; (*c*) $Pr = 50$: $p_4 = 0.52$, $p_5 = 0.37$, $p_6 = 0.05$. The fractions p_i do not add up to one since the values for triangles and heptagons which contribute about 10% are suppressed.

Prandtl number	ε_s^{sim}
35	3.2
40	3.5
45	3.8

TABLE 5. Onset of the hexagon–square transition in the simulation as a function of the Prandtl number. The simulation starts at high ε with a perfect square pattern. On decreasing ε the transition from squares to hexagons occurs at ε_s^{sim} (cf. §5.3).

strong pinning forces of the small-scale structure and can finally lead to the selection of a perfectly regular (square) pattern. This is impossible in the case of an infinite Prandtl number where pinning forces fix defects and grain boundaries.

For even smaller values of Pr we leave the stability domain of hexagons. In figure 11 we observe rolls instead of hexagons which coexist near the threshold of the primary instability with square cells at $Pr = 0.5$. At this Prandtl number the mean flow contributes additional dynamics leading to an intrinsic time dependence in the form of oscillations between both cell types (cf. figure 11*a* and *b*). The remarkable fact coming out of the presented figures is the robustness of the square cells. Although their regularity is modified they appear in STDBC in the entire range of Prandtl numbers studied.

We are now able to sketch a quite complete picture regarding pattern selection in STDBC for different Prandtl numbers. It has been shown in Thess & Bestehorn (1995) that there is a critical value $Pr_c \sim 0.23$, where the flow direction in the centre of the cell turns from downflow to upflow. Below Pr_c inverse hexagons, called g-hexagons (gas), are selected. At $Pr \approx Pr_c$ rolls instead of hexagons are stable near the onset of convection. If ε is increased, time-dependent states follow. For $Pr \gg Pr_c$ ℓ-hexagons (liquid) are stable which are replaced by squares at larger ε. The transition to a regular square pattern is mediated by the mean flow and, therefore, directly linked to a finite Pr. Simulations based on a reduced model (Bestehorn *et al.* 1993) show that defects create a mean flow. In turn, this mean flow forces the defects to start moving and eventually vanishing to leave a perfect square pattern. For $Pr \rightarrow \infty$ ℓ-hexagons are stable near the onset. In the stronger supercritical region irregular patterns occur, probably due to bistability of hexagons and squares. The mean flow is now zero and cannot order the pattern into a regular one.

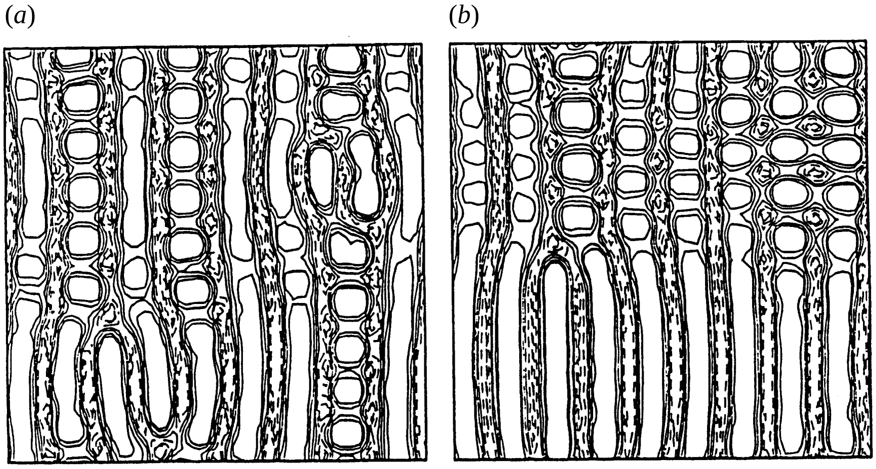

FIGURE 11. Co-existence of squares and rolls ($Pr = 0.5$, $\varepsilon = 0.5$, $Bi_{eff} = 0.1$). At $Pr = O(1)$ rolls instead of hexagons are selected. The region of time-stable patterns shrinks and the onset of weak turbulence already can be found near the threshold. The time dependence is due to the interplay of two sets of rolls perpendicular to each other (*a* and *b*).

5. Heat transport

5.1. *Nusselt number*

In figure 12(*a*) we show the primary measured data in physical units, i.e. heat flux q versus temperature difference $T_b - T_w$. From these data we can infer, using equation (3.7), the actual temperature difference ΔT_l across the liquid layer. Finally, combining (3.7) and (2.17), we calculate Nu, plotted as function of ε in figure 12(*b*).

Looking at figure 12 one recognizes three different regimes, denoted by 1, 2, and 3, distinguished by different slopes. The extent of these regimes is determined by applying linear least-squares fits to the central, visually distinguishable parts of each region, and by defining the transition as the mutual intersection of two linear curves. Range 1 represents the basic quiescent state. This state loses its stability at $(T_b - T_w)_c = 3.39\,\mathrm{K} \pm 0.06\,\mathrm{K}$ ($Pr = 100$, $d_l = 1.43$ mm, $d_g = 0.53$ mm). This value corresponds to a critical temperature difference across the liquid layer $\Delta T_{cd} = 1.16\,\mathrm{K} \pm 0.07\,\mathrm{K}$. ($\Delta T_c = 1.09$ K is predicted by linear theory.) Regime 2 covers the range $0 \leqslant \varepsilon \leqslant 4.22 \pm 0.18$ ($3.39\,\mathrm{K} \leqslant T_b - T_w \leqslant 17.6 \pm 0.2\,\mathrm{K}$). According to figure 7, hexagons are the dominant mode of convection in this regime. Regime 3 is characterized by a significantly increased slope. To understand what happens in this regime we additionally insert in figure 12(*b*) the plot of p_4 against ε. One clearly recognizes the strong correlation between the increase of Nusselt number and the rise in the number of square cells. Figure 12(*b*) constitutes the first measurement of the Nusselt number in STDBC which extends beyond Koschmieder's experimental investigations (Koschmieder & Biggerstaff 1986). In particular, it provides unambiguous experimental evidence for the fact that square cells are more efficient in transporting heat than hexagons.

The different average slopes of the heat flux in the particular regimes are listed in table 6. The behaviour of $\Delta q/\Delta(T_b - T_t)$ in the vicinity of the transition is depicted in the insert of figure 12(*a*). The derivative is calculated via central differences taking into account two neighbouring points on each side. With the appearance of square cells the slope of q starts to increase. Around $T_b - T_t \sim 19.5\,\mathrm{K}$ we observe a weak maximum which correlates with that of the p_5-value. On increasing $T_b - T_t$ further,

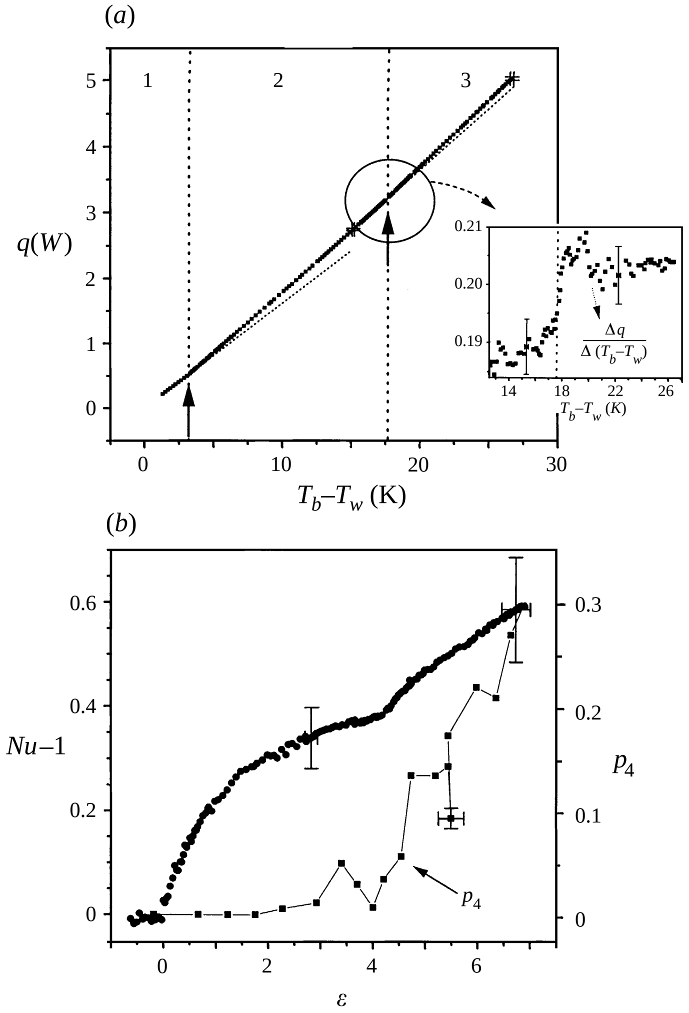

FIGURE 12. (a) Heat flux q, determined from the measured electric power P (cf. §3.1.2), as a function of the measured temperature difference $T_b - T_w$. The insert shows the slope of the heat flux $\Delta q/\Delta(T_b - T_w)$ in the vicinity of the onset of the hexagon–square transition. (b) The Nusselt number Nu and the fraction of square cells p_4 as a function of ε. ($d_l = 1.43$ mm, $d_g = 0.53$ mm, $Bi = 0.52$, $Pr = 100$, $\Gamma = 56$.)

$\Delta q/\Delta(T_b - T_t)$ converges to the value characteristic of the regime dominated by convection in square cells.

The existence of a slope change between regimes 2 and 3 allows the introduction of a second independent measure ε_s^{Nu} for the onset of convection in square cells. Here the superscript Nu indicates the origin of this value from Nusselt number measurements. Making use of all measurements performed with $\Gamma = 56$ we find

$$\varepsilon_s^{Nu} = 4.2 \pm 0.3. \tag{5.1}$$

The error $\Delta\varepsilon = \pm 0.3$ is composed of two parts Δ_1 and Δ_2. The first part, $\Delta_1 = \pm 0.18$ is the standard deviation for the determination of ε (cf. §3.1.2). Although the experiments are conducted under nearly identical conditions, we note a scatter of $\Delta_2 = \pm 0.12$ in the onset of the heat flux increase between independent experimental runs, which

Regime	Characterized by	$\dfrac{\Delta q}{\Delta(T_b - T_w)}$(W K^{-1})
1	Heat conduction	0.162
2	Convection in hexagons and pentagons	0.187
3	Squares, hexagons, pentagons	0.202

TABLE 6. Average slopes of the heat flux in the particular regimes

suggests the existence of a multitude of narrowly spaced dynamical quasi-equilibria. Depending on the noise level, which remains below the threshold of control in the experiment, the system seems to be attracted by one of them.

We are now able to compare the different measures used for characterizing the onset of convection in square cells. In §4.2 we introduced the quantity ε_s^p for the threshold of the systematic increase of the p_4-distribution. We learn from figure 12(*b*) that ε_s^{Nu} and ε_s^p describe the same phenomenon in different words. The change in slope in the heat flux curves can be determined more precisely than the point at which the p_4-distribution starts to rise systematically. Therefore, ε_s^{Nu} is preferred and is henceforth abbreviated as ε_s.

Let us now ask in what manner the numerical simulation supports the experimental observations. To demonstrate the higher efficiency of square cells in the transport of heat without heavy computational effort we solve (3.23), (3.24) for a single regular cell and vary its periodicity length until the maximum Nusselt number is reached. The results are shown in figure 13(*a*). The remarkable point is that the Nusselt numbers belonging to hexagons and squares cross at a value $\varepsilon_x > 0$. Below that value, hexagons transport a higher heat flux, while above it squares possess the larger Nusselt number. This behaviour remains unchanged if we do not maximize Nu because the Nusselt number depends only weakly on the wavenumber k. In a large range, including all experimentally observed wavenumbers, the Nusselt number of a square cell is higher than that of the hexagonal cell provided that $\varepsilon > \varepsilon_x$. The fact that the square cell transports more heat at larger ε is an argument in favour of a secondary instability of hexagons. Clearly, the value of ε_x cannot be compared to the experimental value ε_s. The geometry of the single cell explored in the simulation is entirely determined by the rim. So, both the hexagon and the square are stable at $\varepsilon = 0$, which is not the case in the experiment.

Next we compare in figure 13(*b*) the Nusselt number Nu_6, of the single hexagon, with the Nusselt number Nu of the experiment. Note that the latter quantity is an average value over at least 250 cells whose planform might differ from that of a regular hexagon. In parallel we summarize in table 7 the Nusselt numbers at representative values of ε. We see that in the range $0 \leqslant \varepsilon \leqslant 0.5$ the Nusselt number of the experiment agrees nearly exactly with that of the simulation. With growing numbers of pentagonal cells the Nusselt number of the experiment stays below that of the simulation. So we find a difference of 10% at $\varepsilon = 2$. The reason for this behaviour is the transfer of part of the energy fed to the experimental system to the mean flow generated by the defects. Therefore, the heat flux carried by a cell in the experiment is on average lower than that of the perfectly hexagonal cell in the simulation.

Finally we compare the experimental value ε_s with that predicted by the simulation. In §4.4 we obtained $\varepsilon_s^{sim} = 6.4 \pm 0.6$ from extrapolation to $Pr = 100$. Taking account of the experimental and numerical uncertainties this value exceeds that of the experiment

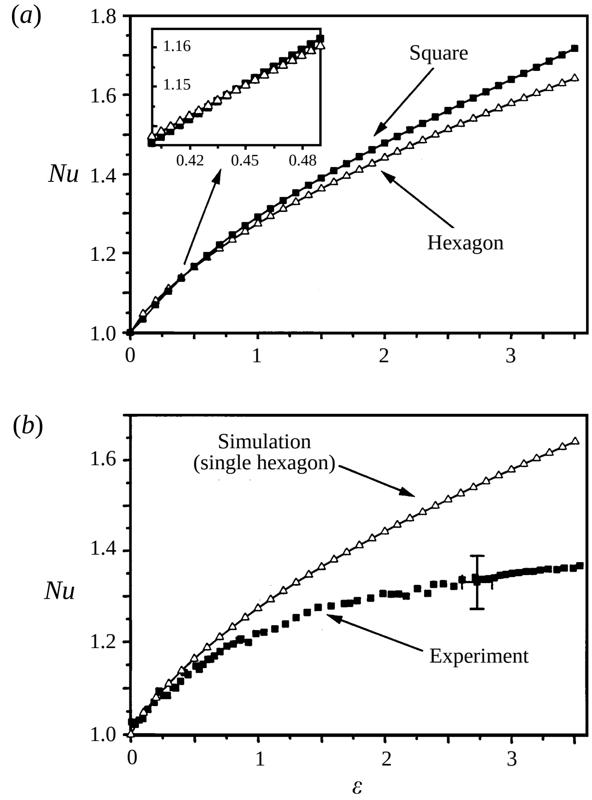

FIGURE 13. (*a*) The Nusselt number obtained by numerical simulation of one elementary hexagonal and square cell, respectively, as a function of ε ($Pr = 100$, $Bi_{eff} = 0.52$). We show the maximum Nusselt number with respect to variation of the wavenumber which is adapted by varying the periodicity length of that cell. (*b*) Comparison between the Nusselt numbers of simulation (single hexagon in *a*) and experiment. The latter curve is identical to that plotted in figure 12(*b*).

	Experiment	Simulation			
ε	Nu	Nu_6	Nu_4	Nu_6^*	Nu_4^*
0.25	1.08	1.095	1.087	1.031	1.028
0.50	1.14	1.163	1.165	1.050	1.051
0.75	1.18	1.221	1.233	1.066	1.069
1.00	1.22	1.274	1.291	1.079	1.084
1.25	1.25	1.338	1.339	1.097	1.095
1.50	1.27	1.365	1.392	1.101	1.107
2.00	1.31	1.444	1.481	1.118	1.125
2.50	1.33	1.516	1.563	1.132	1.141
3.00	1.35	1.583	1.642	1.144	1.154
3.50	1.37	1.646	1.721	1.155	1.167

TABLE 7. Nusselt numbers of experiment and simulation ($Bi = Bi_{eff} = 0.52$). Nu_i with $i = 4, 6$ stands for the Nusselt number of a single square and hexagonal cell, respectively with periodic boundary conditions. Nu^* is the modified Nusselt number frequently used in numerical studies of STDBC. Nu^* is related to Nu via $Nu^* = (1 + Bi)Nu/(Bi + Nu)$ (cf. (2.18)).

by about 30%. The main reason for this difference is the weaker mean flow in the simulation in comparison to the experiment. Inversion of the Laplacian in (3.23*b*), in which the time derivative is set to zero, yields that the mean flow is proportional to Γ^2/Pr where Γ is the aspect ratio. The modes with the smallest damping in simulation and experiment are those whose wavelengths are equal to the periodicity length $L = \Gamma_{sim} d_l$ and to the diameter of the experimental cell $\Gamma_{exp} d_l$, respectively. Consequently, since $\Gamma_{sim} \leqslant \Gamma_{exp}/3$, the numerical mean flow is an order of magnitude smaller than that in the experiment. The mean flow is a necessary ingredient for the hexagon–square transition as was demonstrated in §4.4. Once a defect, like a penta-line, is created within a predominantly hexagonal pattern, the mean flow produced promotes subsequent merging of cell knots in the environment of this aggregate. Merging of cell knots is now the essential step towards the square planform. Thus, the stronger mean flow in the experiment can initiate an earlier onset of the transition. A second reason is the difference in the lateral boundary conditions. In part, the rim is responsible in the experiment for production and absorption of defects. This fact in combination with the foregoing one contributes additionally to the difference in ε_s. Another reason is that buoyancy has been left out of the simulation. The interplay between buoyancy and thermocapillarity is a delicate question that is at present poorly understood. Cerisier *et al.* (1987*a*) showed that the rate of hexagon formation, given random initial conditions (adjusted by stirring at $\varepsilon > 0$), is slowed down with increasing thickness of the layer, i.e. with increasing Rayleigh number. This experiment gives an indication that buoyancy leads to a destabilization of hexagons. This assumption is supported by the bifurcation diagram given by Regnier *et al.* (1997). For this reason, we expect a reduction of ε_s^{sim} if the simulation operates at $\phi \neq 0$ instead of $\phi = 0$.

5.2. *Local temperature differences*

We address the question of to what extent local temperature differences measured by thermoelements reflect the slope changes observed in the heat flux. Before tackling this problem we want to convince the reader that the thermocouples, though introducing a certain disturbance, exert only a weak influence on the pattern formation. In figure 14 we present a shadowgraph of a liquid layer containing three thermocouples, of which only one is visible to the naked eye. From this observation we can infer that pattern selection proceeds largely unaffected by the thermocouples.

Figure 15 shows two data sets taken in different positions inside the system. The data in figure 15(*a*) are a measure of the vertical temperature difference between the liquid bottom and a height of $h = 0.87 d_l$. Figure 15(*b*) represents the temperature difference across the air layer up to a distance of $0.06 d_l$ below the free surface. In agreement with the heat flux measurements we identify three regimes characterized by different slopes. Ranges 1 and 2 represent again the pure conductive state and the regime dominated by convection in hexagonal cells, respectively. The important feature of both curves is the second change in slope, leading to regime 3. To understand what happens in 3, one has to investigate in which cell planform the thermoelements are placed. Tracing its location in the shadowgraph images one finds that in the initial stage of regime 3 the thermoelement faces a pentagonal cellular environment. This pentagon soon becomes elongated into a non-regular planform and successively transformed into a square one.

We can infer from the observed slope changes a changed deformation of the isotherms. Generally, any increase of the convective heat flux shifts an isotherm in the region of rising (falling) liquid in the direction of the free surface (liquid bottom).

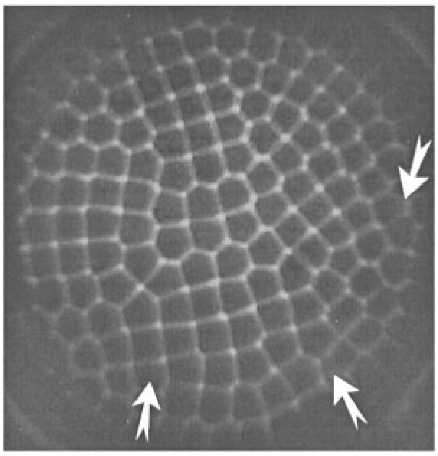

FIGURE 14. Shadowgraph image of a liquid layer containing three thermocouples, whose locations are indicated by arrows. Only one of them (below right) is visible to the naked eye.

If a vertical temperature difference across a certain distance in the upstreaming liquid experiences a slower growth, as a function of the temperature difference across the liquid layer (cf. figure 15*a*), we can conclude that there is a stronger heat flux transported in this regime. In turn, the averaged temperature difference across the remaining height of the liquid–air system must increase at the same time (cf. figure 15*b*). Thus, both curves show that a square cell possesses, in the vicinity of the free surface, a stronger steepening of the temperature gradient in the region of upstreaming liquid. This higher efficiency of a square cell for transporting heat is already anticipated by a non-regular pentagon.

Next we want to clarify the location of the slope changes in the thermoelement signals relative to the heat flux. In five of six independent runs we find that the break in the slope occurs in the thermoelement signals at higher ε compared with the heat flux. This shift can extend up to $\Delta\varepsilon = +0.8$. In only one case did we note a parallel onset. The delay corresponds to the picture of a continuous transformation of hexagonal into square cells over the intermediate pentagonal planform. The transformation proceeds in different parts of the container with different speeds.

Thus, the measurements of local temperature difference clearly support the results of the preceding sections. A comment is required to define the term ‘local’. While the position of the two thermoelement wires is fixed inside the two-layer system, the convective pattern is not completely stationary. We are faced with two consequences. First, upstream and downstream regions can move through the thermoelement. This would manifest itself in fluctuations of the signal which, indeed, can be observed in both curves. In parallel, we know that the probability of finding a thermocouple in regions of the rising liquid soon becomes distinctly higher, because the upflow occupies more and more of the space of the cell with increasing ε (Thess & Orszag 1995). Second, travelling of cells with different planform through the thermoelement could cause a misinterpretation of the signals, especially in regime 3. By carefully studying the cellular environment around the thermoelement we can definitely exclude this possibility in figure 15.

The numerical simulation enables us to develop a picture of the temperature fields inside a convection cell. In figure 16 (a, b) (c, d) we show the contour plots of Θ in a hexagonal and square cell respectively. These plots result from a simulation of a

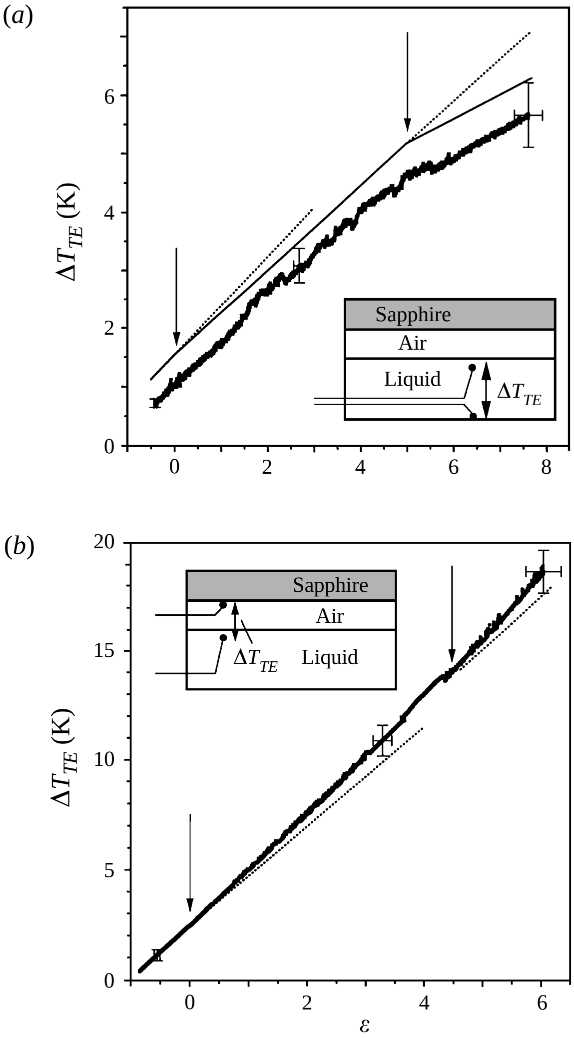

FIGURE 15. Local temperature measurements. (*a*) The temperature difference ΔT_{TE} in the liquid layer between the bottom and a height $h = 0.87d_l$. ($d_l = 1.45$ mm, $d_g = 0.51$ mm, $\Gamma = 56$, $Pr = 100$. Convection sets in at $\Delta T_c = 1.08$ K). (*b*) Temperature difference ΔT_{TE} between the underside of the sapphire disc and a point located in the liquid $0.06d_l$ below the surface. ΔT_{TE} is thus nearly the temperature drop across the air gap. ($d_l = 1.44$ mm, $d_g = 0.52$ mm, $\Gamma = 56$, $Pr = 100$. Convection sets in at $\Delta T_c = 1.12$ K). The precise location of the thermoelements is illustrated in inserts.

unit cell with periodic boundary conditions (see §4.3). A common property of both cell types is that the regions where the cold liquid goes down becomes smaller with increasing ε. Studying one-dimensional plots of $\Theta(z)$ at points at the surface where Θ reaches its maximum (minimum) value, we find a significant asymmetry between upflow and downflow established for both types of cells. This asymmetry becomes more pronounced with increasing ε. If we divide the one-dimensional plot of the points of maximum (minimum) $\Theta(z)$ of a hexagon by the corresponding plots of a square, we see marked deviations between the cell types especially in the region of downflow. The difference between the maxima and minima at different heights is stronger for cells with square symmetry.

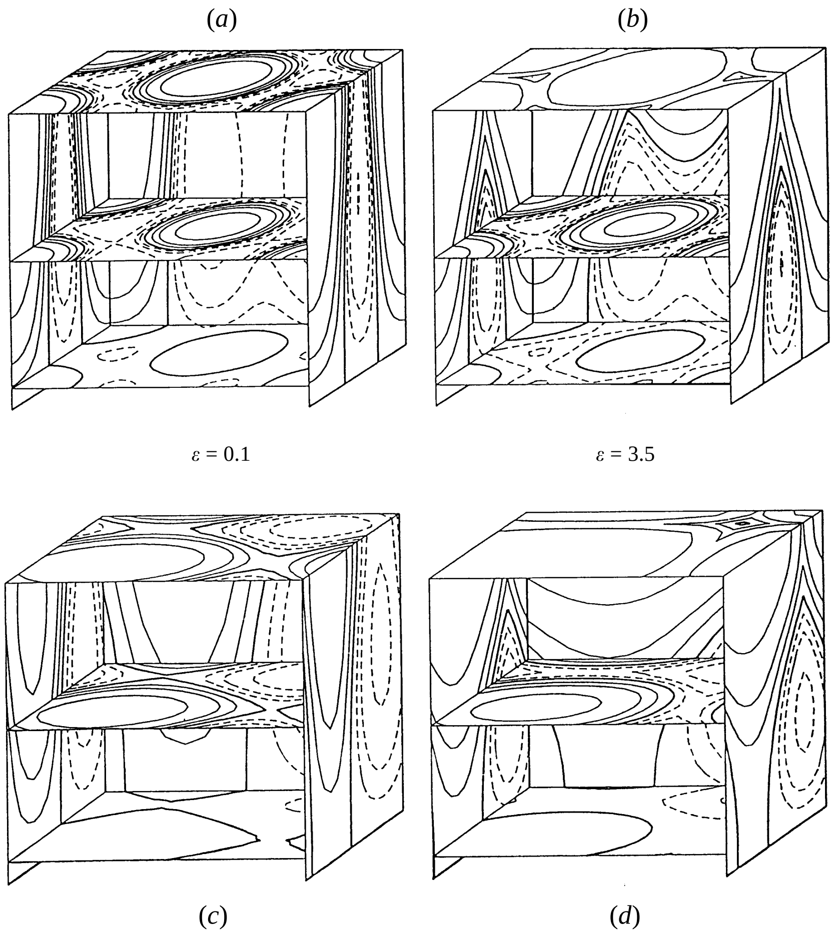

FIGURE 16. Stationary pattern found from numerical integration of the three-dimensional one-layer problem. Plotted are the contour lines of the deviation Θ of the temperature from the conductive state near the threshold (left) and far above (right). The values for Θ are 0 (bold), $\Theta_{max}/8$, $\Theta_{max}/4$, $\Theta_{max}/2$ (solid), and $\Theta_{min}/8$, $\Theta_{min}/4$, $\Theta_{min}/2$ (dashed). (*a, b*) The lateral aspect ratio (L_x/L_y) is $\sqrt{3}$ and one *hexagon* fits exactly into the cell. (*c, d*) The lateral aspect ratio is 1 which leads to the formation of a *square cell*. With increasing ε the colder areas on the surface shrink. Consequently, the mean interface temperature increases in comparison to the conductive state. This is an expression of the higher heat flux transferred by the cell.

We finally list in table 8 some typical values for the amplitudes of temperature perturbation and velocity at the surface. These values are obtained from numerical simulations with $\Gamma = 23$ after averaging over all cells.

5.3. *Hysteresis*

While many properties of the transition have been understood, we do not know anything yet about its bifurcation type. To specify whether the hexagons–square transition is of subcritical or supercritical type we examine the changes occurring in the system between runs with increasing ε and those with decreasing ε. This is done both experimentally and numerically.

In the experiment special care is taken to achieve a pattern sparse in defects in the vicinity of the threshold for the transition. The temperature difference is changed by

ε	θ_{max} (K)	v_{max} (10^{-2} m s^{-1})
1.0	1.0	0.14
2.0	1.7	0.21
3.0	2.6	0.26

TABLE 8. Maximum values of temperature perturbation and velocity at the free surface at different ε

the same rate of 0.08 K h^{-1} during the upward and the downward run, respectively. On plotting the relative cell numbers in figure 17(*a*) we find that the number of squares [hexagons] at the same ε is higher [lower] in the downward run than in the upward one. This fact is related to a shift of the maximum pentagon number in the downward run towards lower ε. From the measurement of the Nusselt number, we find that square cells can be preserved up to $\Delta\varepsilon = -0.4 \pm 0.1$ below ε_s.

Next we ask whether the numerical simulation confirms the hysteresis found in the experiment. To keep the computation time efficient it is useful to reduce the Prandtl number from 100 to 40. As shown in §4.4 this can be done without loss of generality. The hysteresis loop obtained from simulation is shown in figure 17(*b*). Starting with a regular square pattern at large ε we find the transition to hexagons to occur at $\varepsilon_s = 3.5$. This is accompanied by a jump in the Nusselt number. In the reverse direction the hexagons become unstable to square cells at $\varepsilon = 4.0$. The hysteresis extends to $\Delta\varepsilon = -0.5 \pm 0.1$ which agrees well with the value found in the experiment. From the fact that the hexagon–square transition involves hysteresis we can conclude its subcritical nature. Within the analogy to first-order phase transition the pentagon plays the role of a crystallization nucleus.

6. Time dependence

It is natural to ask whether the nearly stationary state, which is typical of the hexagonal pattern formed after the primary instability, is maintained in the system when it undergoes the secondary instability. In order to answer this question we have conducted a long-time experiment at $\varepsilon = 4.8$ covering more than 60 units of the horizontal diffusion time τ_h which corresponds to 16 days of real time. In figure 18 we plot six shadowgraph images taken at intervals of 24 hours (*a*–*c*) and 2 hours (*d*–*f*) or equivalently 4.2 and 0.4 units of τ_h. Figure 18 gives a vivid impression of the time dependence in the transitional region, and in particular of the persistent irregularity on two different temporal scales and a large spatial scale. As an example of the processes taking place on a large temporal scale (figure 18, left) we turn to the transformations occurring at the left upper part of the container (see arrow). In figure 18(*a*) one recognizes a domain of well-ordered hexagonal cells. In figure 18(*b*) a larger number of these hexagons already have been converted into pentagons. The process advances, as seen in figure 18(*c*). Only a small number of hexagons survive in the selected area. The scene is dominated by pentagons and squares. A reversal of this transformation process can be observed in other areas. The behaviour found on a large time scale is encountered in a similar manner on a short time scale. Let us focus on the right lower part of figure 18(*d*). One sees a fairly extended hexagonal domain. In the course of time (figure 18*e* and *f*) it becomes more and more intersected by square domains which are surrounded by chains of pentagons.

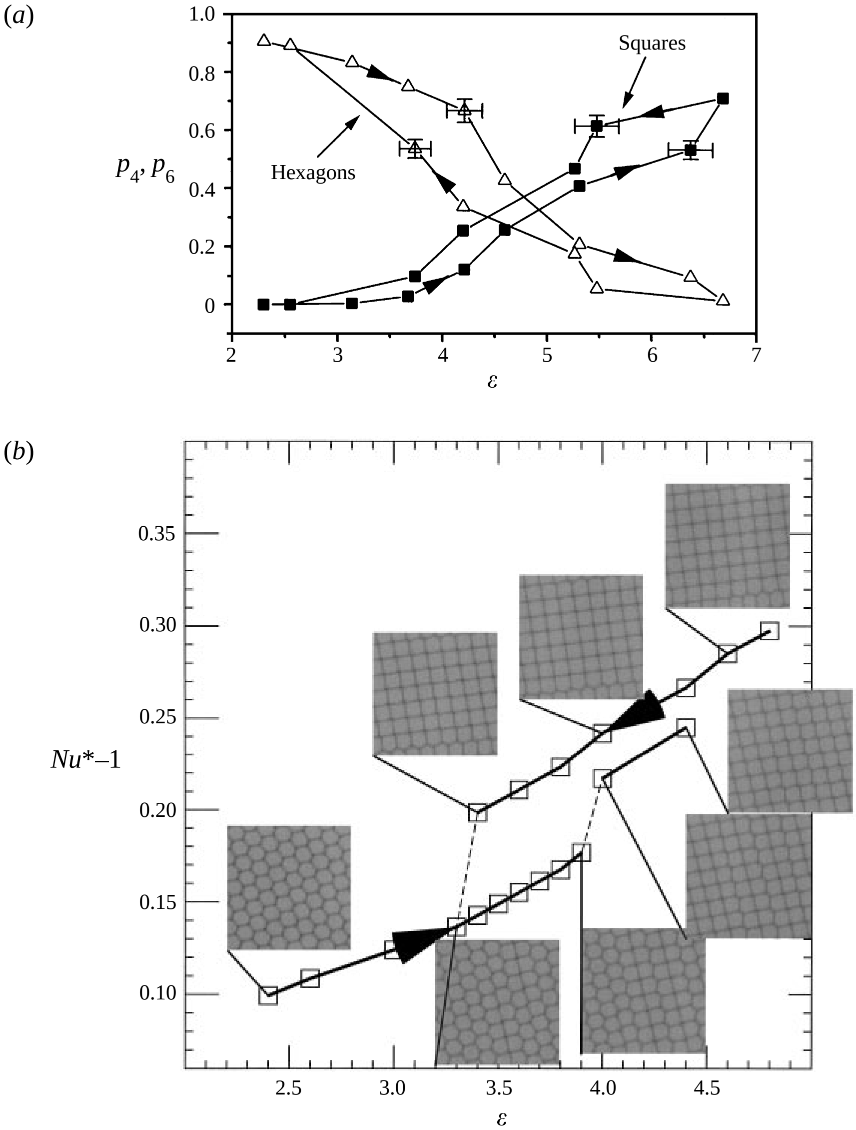

FIGURE 17. Hysteresis. (*a*) Fraction of hexagons p_6 and squares p_4, respectively, as a function of growing/falling ε as observed in the experiment. (*b*) Hysteresis loop at $Pr = 40$ as obtained from simulation. Coming from large ε with an almost regular square pattern, the Nusselt number (Nu^*) clearly jumps at about $\varepsilon = 3.5$ to a lower value typical of a hexagonal configuration. If ε is increased, the number of pentagons arranged in the penta-lines increases and another jump can be seen at $\varepsilon = 4$ after which the structure is again dominated by squares. The loop is not completely closed since small dislocations remain stable, probably due to pinning effects of the periodic lateral boundary conditions.

In figure 19 we plot the temporal evolution of the angular displacement of the three (two) main peaks in wavenumber space belonging to subsections of the patterns that contain only hexagons (squares). We get these quantities by applying a procedure which was described in §3.1.3. Since the hexagonal and the square part of the pattern, respectively, are built up of domains of different orientation, the spectrum can contain

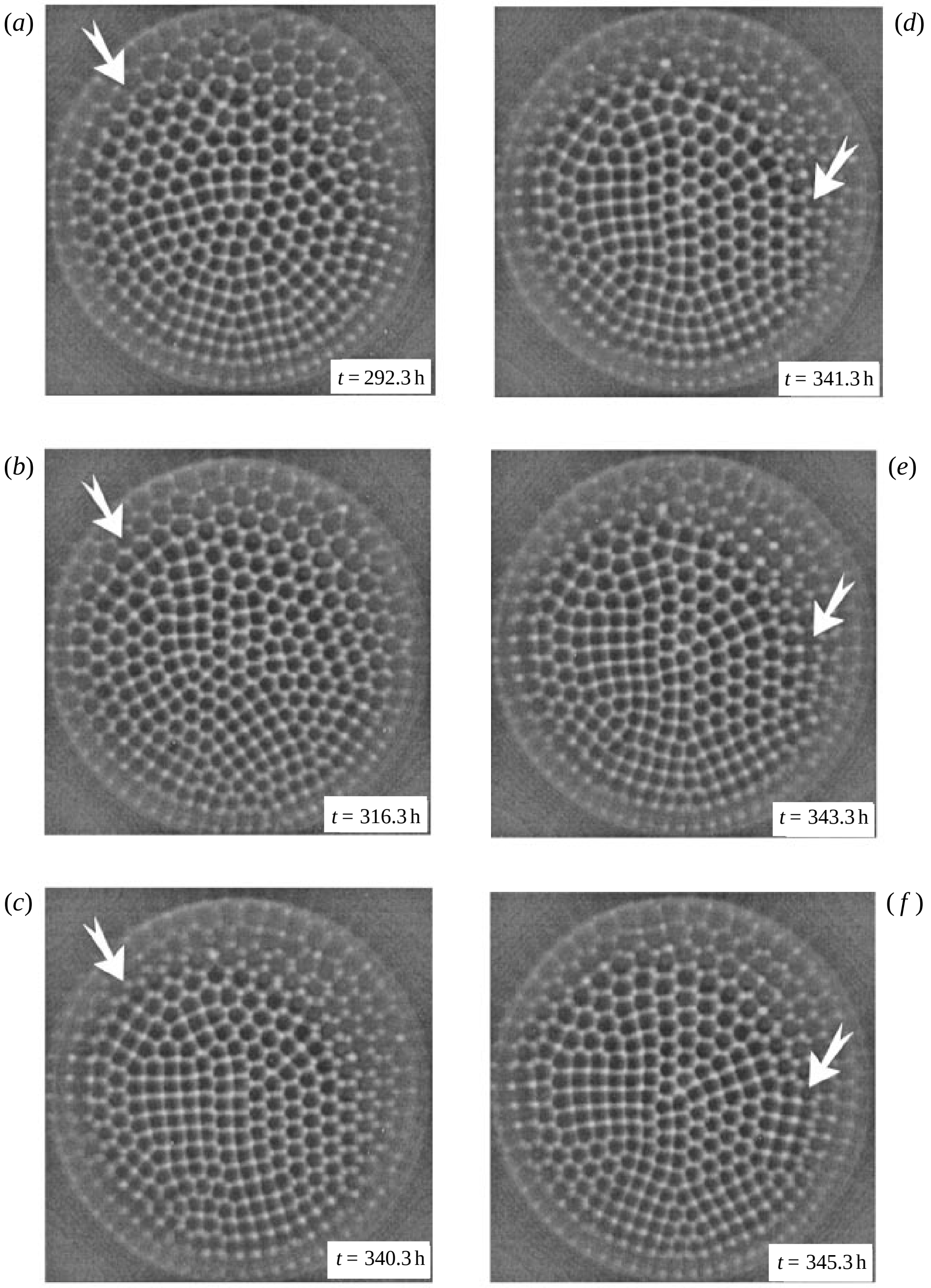

Figure 18. Time-dependent Bénard convection: shadowgraph images taken every 24 hours (*a–c*) and every 2 hours (*d–f*) from an experiment of long duration. Parameters are $\varepsilon = 4.8$, $\Gamma = 64$, $d_l = 1.41$ mm, $d_g = 0.26$ mm, $Pr = 100$, $\tau_h = 5.6$ h.

more than four (square cells) or six (hexagonal cells) basic modes. In the case of clearly separated peaks we use the pairwise largest peaks as the basic modes. If we find two or more narrowly located sub-peaks we take the first moment of these sub-peaks as representative of the basic mode. On the time scale on which we have studied the

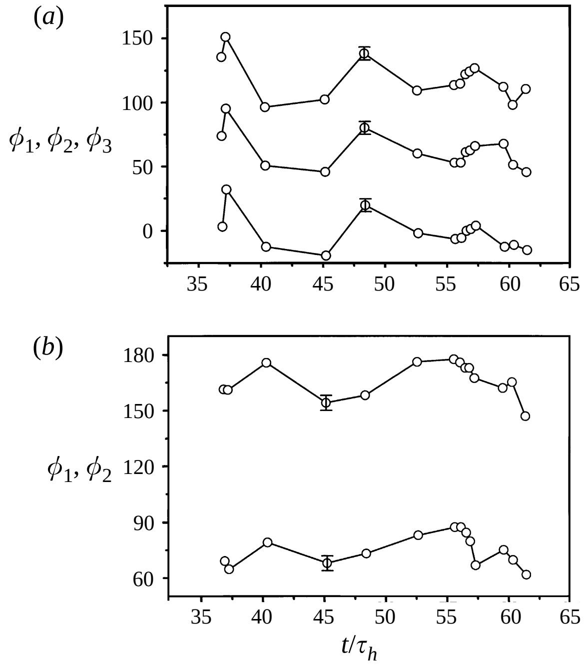

FIGURE 19. Time dependence of the angular positions of the main Fourier peaks in a hexagonal (*a*) and a square (*b*) subdomain of the pattern. Parameters as in figure 18.

structure we find an erratic rather than periodic behaviour of these basic modes. One recognizes, further, that the movement of the dominant cell domains of a given symmetry cannot strictly be considered as the movement of a rigid body. Slight deviations in the temporal behaviour between the basic modes can be found. This is a hint of local stresses leading to the deformation of the cell domain. The internal deformation is particularly pronounced between $t = 40\tau_h$ and $t = 45\tau_h$ in figure 19(*a*) and between $t = 55\tau_h$ and $t = 60\tau_h$ in figure 19(*b*).

A second observation is that the hexagonal and the square cell domains obey different time dependences. This is particularly visible at $t = 55\tau_h$, where a local minimum in the ϕ_i of the hexagonal modes coincides with a maximum in the ϕ_i of the square modes. A minimum (maximum) in the angular location equals a rotation away from the average position in the clockwise (counterclockwise) direction. So we can interpret this behaviour as a kind of counter-rotation of cell domains with different symmetry. As a consequence, the angle between a particular mode of the hexagonal domain and that of the square domain becomes larger while other modes of the corresponding domains come closer together. This means that hexagonal and square domains move towards a common symmetry line. This counter-rotation could be one possible Fourier-space representation of the elementary process underlying the transformation.

We return to the physical space and plot in figure 20 the change in the composition of the pattern as a function of time. The fraction p_i of cells of a particular planform undergoes fluctuations of up to 7% of its average value. This is an expression of a permanent transformation from one cell planform into another one. While in the interval $t = (37\dots50)\tau_h$ the planform fluctuations between hexagons and pentagons occur at nearly constant p_4, we notice between $t = (50\dots60)\tau_h$ a crossover

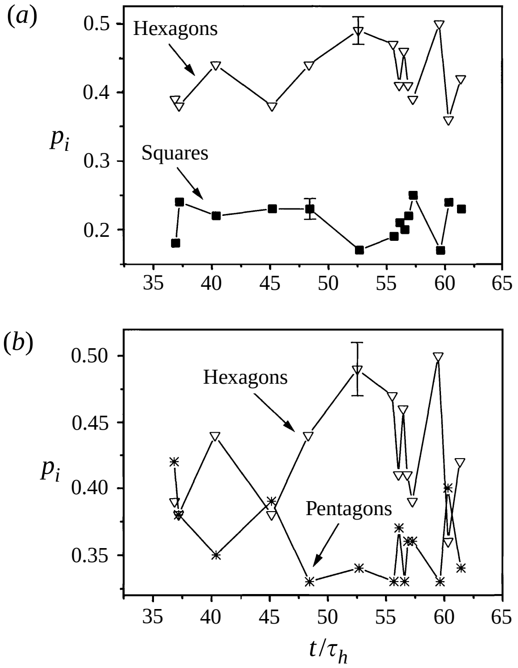

FIGURE 20. Time dependence of the cell fractions $p_i (i = 4, 5, 6)$ as obtained from the experiment of long duration. Same parameters as in figure 18.

to fluctuations between squares and hexagons at nearly constant p_5. Figure 20 supports the idea that counter-rotation might be a Fourier-space translation of the elementary transformation process. Slightly above $t = 55\tau_h$ we find the p_6-decrease to be correlated with a p_4-increase. In figure 19 we have identified in this time interval the maximum degree of counter-rotation between hexagonal and square domains.

Before we discuss the sources of the time-dependent behaviour found in the experiment we ask what happens in the simulation. In figure 21 a time series at large $\varepsilon = 11$ is shown for $Pr = 20$. Square cells are the dominating planform although some defects are present. These are mainly localized in the middle right part of each picture. At a first glance, similar processes as observed in the experiment take place around these regions. Cells of different planform transform permanently into each other. The marked difference to the experiment at $Pr = 100$ consists, however, in the non-stationarity of the square cells. This phenomenon is illustrated in figure 22 which shows a quadruple of cells. The central cell knot of the quadruple (figure 22*b*) splits into two narrowly spaced cell knots which move along the line drawn in figure 22(*a*). Consequently, one pair of cells retains its square planform while the other pair gets an additional edge. If a certain edge length is reached the motion is reversed. Half of the period of the oscillation is completed when the two cell knots have merged once more. Then, this process starts again, but the direction of motion jumps by an angle of 90°. This type of non-stationary square only occurs in a limited range of Prandtl numbers. By $Pr = 40$ the squares are stationary at the same $\varepsilon = 11$. The domains of square cells are surrounded by defects. After passing through a transient the entire pattern becomes stationary at this Prandtl number, too.

This result does not contradict to the time dependence found in the experiment at $Pr = 100$ since experiment and simulation differ in two important aspects. First,

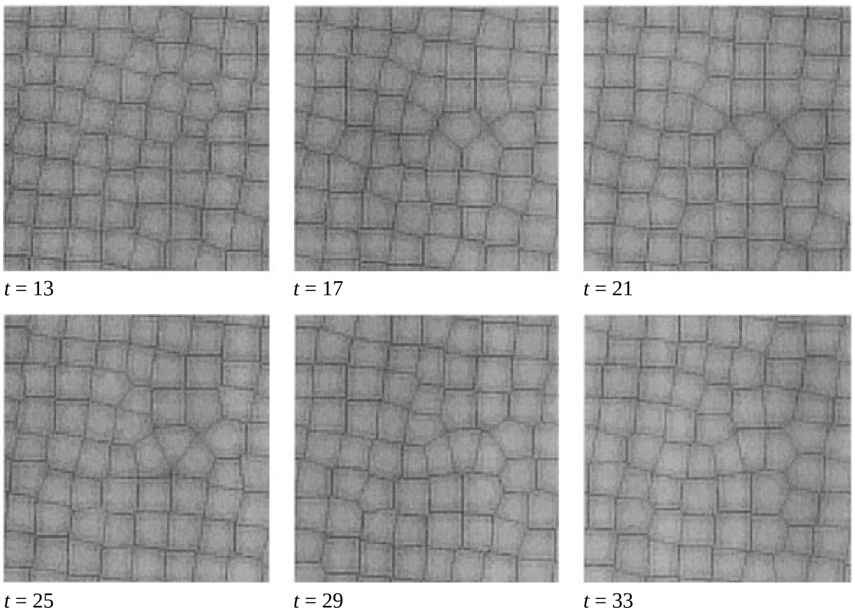

FIGURE 21. Time-dependent Bénard convection in numerical simulation. Plotted are the isotherms with increasing integration time at $\varepsilon = 11$ and a Prandtl number $Pr = 20$. The square cells display a special type of non-stationarity which is explained in figure 22. Between the three cell planforms permanent transitions take place.

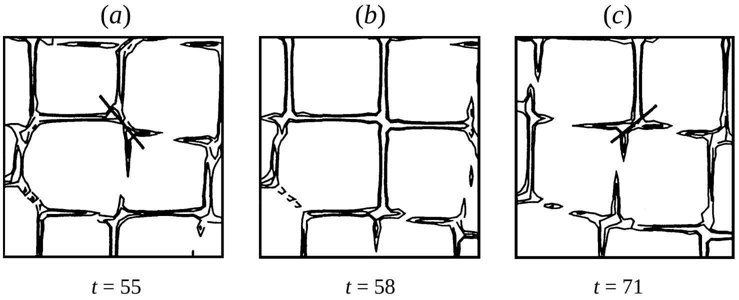

FIGURE 22. Non-stationary square cells at $Pr = 20$: Periodic splitting and merging of cell knots in a square subdomain. The equilibrium position around which the oscillation occurs is shown in (*b*). By splitting of the central cell knot (*b*) two new cell knots are produced which move along the line drawn in (*a*). The new edge does not extend beyond a certain length, at which extent of separation the direction of motion is reversed, leading to repeated merging of both cell knots. The process starts again, whereby the direction of motion is now rotated by an angle of 90° (*c*).

the higher aspect ratio of the experiments admits a larger number of degrees of freedom. Second, the periodic boundary conditions do not take into account the natural geometry of the experiment. Nevertheless, we have to find the sources of the time dependence in the experiment. The main contribution, analogously to the simulation, is the mean flow generated by the defects in the pattern. In the first place these are the pentagons which separate hexagonal and square domains. At the front of the pentagons, directed towards the hexagonal cells, the mean flow promotes further merging of cell knots. At the opposite side, directed towards the squares, it again supports the splitting of cell knots. These processes are equivalent to the transformation of one cell class into another one. The transformations proceed with different intensity in experiment and simulation because the mean flow in the simulation is clearly weaker. As discussed in §5.1 the mean flow in the simulation is proportional to L^2/Pr where L is the periodicity length. Since L is considerably smaller than the diameter of the experimental container, the numerical mean flow experiences a stronger damping than that in the experiment. This effect makes plausible why the time dependence is expected to subside in the simulation at lower Prandtl number than in the experiment.

A second contribution to the time dependence comes, as correctly argued by one of the referees, from a non-homogenous pinning of the contact line to the Plexiglas ring. To estimate this effect we replace the projector within our optical arrangement by a HeNe-laser. In general, we observe at two places at the Plexiglas ring a significant shift of the Fizeau fringes resulting from interference between the bottom and the sapphire window. At $T_b - T_w = 0$, this non-uniformity amounts to 15-25 fringes which equals 4–8 μm. The tangential extent of these regions is about 5-10 mm. The extent normal to the wall is smaller than 3 mm which corresponds to the capillary length $\delta = (\sigma/\rho_l g)^{1/2} = 1.5$ mm of the liquid. In the course of the experiment the location of the regions with non-perfect pinning remains fixed while the non-uniformity becomes stronger with increasing ε. The temperature perturbation caused by such a region gives rise to a secondary STD flow in the immediate vicinity of the wall. Depending on the direction of the velocity vector, relative to the tangential vector of a cell edge, this secondary flow can again promote the merging/splitting of cell knots. In this way the perturbation can cause dynamics near the wall which is in some sense similar to that forced by the mean flow. Due to the limited extent of the perturbed regions, however, the secondary flow influences directly not more than three cells near the wall. Planform changes of these cells of course can modify the shape of cells over a smaller area. But it is unlikely that this rather short-ranging mechanism is responsible for the time dependence in regions located 60–80 mm away from the places of non-homogenous pinning of the contact line.

7. Conclusions

We have studied the evolution of surface-tension-driven Bénard convection cells up to $\varepsilon = 8$ by a combination of accurate experiments and high-resolution three-dimensional simulation. We find that sufficiently far from the threshold for onset of the primary instability hexagonal cells lose their stability in favour of convective cells with square planform. Experimental observation shows that this secondary instability occurs at $\varepsilon_s = 4.2 \pm 0.3$ ($Pr = 100$). This value is about 35% smaller than that predicted by the simulation. The bifurcation is subcritical, which follows from the observed hysteresis. Experiment and simulation yield nearly the same subcriticality of $\Delta\varepsilon = -0.5 \pm 0.1$. The transition from hexagons to squares is accompanied by an increase of the Nusselt number. In the experiment we find a strong correlation between the increase of the number of square cells and the change in slope of both heat flux and temperature drop in the upflow measured by small thermocouples. From this observation it follows that square Bénard cells are indeed the more efficient mode of heat transfer than hexagonal cells beyond ε_s. This fact is confirmed by numerical simulations of both medium aspect ratios and elementary cells of hexagonal and square planform, respectively. Studying experimentally the wavenumber of hexagonal and square cells we find by two independent approaches that square cells possess a wavenumber which is about 8% higher than that of hexagonal cells. The numerical simulations show that the Prandtl number plays an important role within the hexagon–square transition. On decreasing the Prandtl number the onset of the transition is shifted towards smaller ε_s. In parallel, the square cells become more and more organized in regular domains. At $Pr = O(1)$ the coexistence between hexagons and squares is replaced by a competition between rolls and squares.

The transition from hexagons to squares is mediated by pentagonal cells. Within the transitional regime, characterized by the presence of all three planforms, the experimental system exhibits complex irregular dynamics. Numerical simulation displays qualitatively similar dynamics which is, however, restricted to the Prandtl number range $25 \leqslant Pr \leqslant 40$. Beyond $Pr = 40$ the pattern is stationary. Below $Pr = 25$, the square cells become non-stationary which is manifested in periodic merging and splitting of cell knots. We see two reasons for the difference between experiment and simulation with respect to the Prandtl number beyond which time-dependent behaviour vanishes. First, the mean flow in the simulation is dampened considerably more strongly than the experiment. Second, in the lateral boundary conditions of the experiment there are residual imperfections which are below the threshold of control. These imperfections are caused by a non-homogeneous pinning of the meniscus along the rim of the container. The temperature perturbation arising from this effect gives rise to a secondary STD flow. In the immediate vicinity of the wall this flow has dynamics comparable to that produced by the mean flow. It is however unlikely that this rather short-ranging mechanism is responsible for the dynamics observed in the central parts of the container. Moreover, the virtual source for this dynamics is the mean flow, mainly produced by the pentagonal patches of the pattern. In the hexagonal cells at the front of the pentagons the mean flow supports further merging of cell knots. At the back, directed towards the squares, it again supports the splitting of knots. In this way it leads to the slow fluctuations in the cell numbers p_i which are observed.

The weaker mean flow in the simulation should also be one reason for the difference in the values of ε_s. Once a defect appears, e.g. a pentagon, the mean flow supports the continuation of merging of cell knots in the neighbouring hexagonal cells. The stronger mean flow is expected to trigger an earlier onset of the transition in comparison to the simulation. An additional source of the difference is the buoyancy which has been left out of the simulation. On the basis of previous experiments of Cerisier *et al.* (1987*b*) and a recent work of Regnier *et al.* (1997), discussed in §5.1, we infer an earlier onset of the transition in simulations performed at $\phi \neq 0$. A more detailed study of the effect of buoyancy on STDBC is in preparation. Another reason for the deviation may arise from the fact that simulations relying on the Boussinesq assumption are compared with experiments in a liquid whose material properties are not strictly constant. The main non-Boussinesq contribution in the experiment comes from the temperature dependence of the liquid viscosity. For the maximum value of $\varepsilon \sim 8$ we obtain

$$\gamma_2 = \frac{\nu_l(T_b) - \nu_l(T_b - (\varepsilon + 1)\Delta T_c)}{\bar{\nu}_l} = -0.14$$

where $\bar{\nu}_l$ is the average value of the viscosity at the bottom and at the interface. Since STDBC has no theory incorporating non-Boussinesq effects we consult the theory for non-Boussinesq RBC (Busse 1967). From this theory we obtain an asymmetry factor $\mathscr{P} \sim P_2\gamma_2 = -0.4$. This value is small in comparison to the deviations found usually in RBC under non-Boussinesq conditions (cf. Walden & Ahlers 1981; Pampaloni *et al.* 1992). Moreover, non-Boussinesq effects are expected to shift ε_s towards higher values since the hexagonal mode of convection is stabilized due to the stronger top-down asymmetry. However, the experimental value of ε_s lies below that predicted by the Boussinesq simulation. From that fact, together with the small asymmetry factor $\mathscr{P}$, one can infer that non-Boussinesq effects are of minor importance in our system.

A comment is apposite regarding the integration of the hexagon–square transition into the variety of pattern-formation processes in hydrodynamics. The hexagon–square transition in STDBC is markedly different from other transitions which have been studied so far. Square cells are predicted at onset of RBC in the case of thermally insulating boundaries (Busse & Riahi 1980) and for convection with solidification (Hadji, Schell & Riahi 1990). Experimentally, square patterns have been observed in binary-liquid convection (Le Gal, Pocheau & Croquette 1985; Moses & Steinberg 1986), in RBC with strongly temperature-dependent viscosity (Oliver 1983; White 1988) or at constant viscosity and high Rayleigh numbers (Whitehead & Parsons 1978). However, none of these documented square patterns evolve from a hexagonal planform, as in our case. In contrast to the competition between hexagons and rolls, in RBC with non-Boussinesq effects (Ciliberto, Pampaloni & Pérez-Carcía 1988; Pampaloni *et al.* 1992), and between hexagons and rolls, or squares and rolls, in solidification problems (Davis, Müller & Dietsche 1984; Karcher & Müller 1995; Hadji *et al.* 1990), a third pentagonal planform is involved in our transition.

While many aspects of the hexagon–square transition, such as the higher Nusselt numbers and wavenumbers of square Bénard cells and the Prandtl number influence are understood, a number of points remain unanswered. Among these are the time dependence, the fine structure of flow and temperature fields and finally the question of what happens after the square cells. Further, we wish to remark that non-Boussinesq STDBC is worth studying because of its impact on modern technologies, such as material processing with electron or laser beams.

We are grateful to E. L. Koschmieder, Ch. Karcher, C. Pérez-García and Th. Boeck for stimulating discussions, to A. Golovin for communicating his results prior to publication, to S. Erlebach for designing a part of the electronics and to S. Bruhns for his help with experimental issues. K.E. and A.T. acknowledge financial support from the Deutsche Forschungsgemeinschaft (Grant Th497/8-1) and from the Sächsisches Staatsministerium für Wissenschaft und Kunst.

REFERENCES

Bénard, H. 1900 Les tourbillons cellulaires dans une nappe liquide. *Rev. Gén. Sci. Pures Appl.* **11**, 1261–1271.

Bestehorn, M. 1993 Phase and amplitude instabilities for Bénard–Marangoni-convection in fluid layers with large aspect ratio. *Phys. Rev.* E **48**, 3622–3634.

Bestehorn, M. 1996 Square patterns in Bénard-Marangoni convection. *Phys. Rev. Lett.* **76**, 46–49.

Bestehorn, M. Fantz, M. Friedrich, R. & Haken, H. 1993 Hexagonal and spiral patterns of thermal convection. *Phys. Lett.* A **174**, 48–56.

Block, M. J. 1956 Surface tension as the cause of Bénard cells and surface deformation in a liquid film. *Nature* **178**, 650–651.

Boeck, Th. & Thess, A. 1997 Inertial Bénard–Marangoni convection. *J. Fluid Mech.* **350**, 149–175.

Bragard, J. & Lebon, G. 1993 Non-linear Marangoni convection in a layer of finite depth. *Europhys. Lett.* **21**, 831–836.

Busse, F. H. 1967 On the stability of two-dimensional convection in a layer heated from below. *J. Math. Phys.* **46**, 140-149.

Busse, F. H. 1981 Transition to turbulence in Rayleigh–Bénard convection. In *Hydrodynamic Instabilities and the Transition to Turbulence* (ed. H. L. Swinney & J. P. Gollub). Springer.

Busse, F. H. & Riahi, N. 1980 Nonlinear convection in a layer with nearly insulating boundaries. *J. Fluid Mech.* **96**, 243–256.

Busse, F. H. & Whitehead, J. A. 1971 Instabilities of convection rolls in a high Prandtl number fluid. *J. Fluid Mech.* **47**, 305–320.

Busse, F. H. & Whitehead, J. A. 1974 Oscillatory and collective instabilities in large Prandtl number convection. *J. Fluid Mech.* **66**, 67–79.

Chandrasekhar, S. 1961 *Hydrodynamic and Hydromagnetic Stability*. Oxford University Press.

Cerisier, P., Jamond, C., Pantaloni, J. & Charmet, J. C. 1984 Déformation de la surface libre en convection de Bénard–Marangoni. *J. Phys. Paris* **45**, 405–411.

Cerisier, P., Jamond, C., Pantaloni, J. & Pérez-García, C. 1987*a* Stability of roll and hexagonal patterns in Bénard–Marangoni convection. *Phys. Fluids* **30**, 954–959.

Cerisier, P., Pérez-García, C., Jamond, C. & Pantaloni, J. 1987*b* Wavelength selection in Bénard–Marangoni convection. *Phys. Rev.* A **35**, 1949–1952.

Cerisier, P., Pérez-García, C. & Occelli, R. 1993 Evolution of induced patterns in surface tension-driven Bénard convection. *Phys. Rev.* E **47**, 3316–3325.

Ciliberto, S., Pampaloni, E. & Pérez-García, C. 1988 Competition between different symmetries in convective pattern. *Phys. Rev. Lett.* **61**, 1198–1201.

Cloot, A. & Lebon, G. 1984 A nonlinear analysis of the Bénard–Marangoni problem. *J. Fluid Mech.* **145**, 447–469.

Dauby, P. C. & Lebon, G. 1996 Bénard–Marangoni instability in rigid rectangular containers. *J. Fluid Mech.* **329**, 25–64.

Davis, S. H. 1987 Thermocapillary instabilities. *Ann. Rev. Fluid Mech.* **19**, 347–359.

Davis, S. H., Müller, U. & Dietsche, C. 1984 Pattern selection in single-component systems coupling Bénard convection and solidification. *J. Fluid Mech.* **144**, 133–151.

Eckert, K. 1997 Von hexagonalen zu quadratischen Konvektionszellen: Experimentelle Untersuchungen zur oberflächenspannungsgetriebenen Bénard-Konvektion. PhD dissertation, Otto-von-Guericke-University of Magdeburg.

Gollub, J. P. & McCarriar, A. R. 1982 Convection in Fourier space. *Phys. Rev.* A **26**, 3470–3476.

Golovin, A. A., Nepomnyashchy, A. A. & Pismen, L. M. 1997 Nonlinear evolution and secondary instabilities of Marangoni convection in a liquid-gas system with deformable interface. *J. Fluid Mech.* **341**, 317–341.

Hadji, L., Schell, M. & Riahi, D. N. 1990 Interfacial pattern formation in the presence of solidification and thermal convection. *Phys. Rev.* A **41**, 863–873.

Karcher, Ch. & Müller, U. 1995 Convection in a porous medium with solidification. *Fluid Dyn. Res.* **15**, 25–42.

Kittel, Ch. 1966 *Introduction to Solid State Physics*. John Wiley & Sons.

Koschmieder, E. L. 1967 On convection under an air surface. *J. Fluid Mech.* **30**, 9–15.

Koschmieder, E. L. 1991 The wavelength of supercritical surface-tension-driven Bénard convection. *Eur. J. Mech.* B/*Fluids* **10**, 233–237.

Koschmieder, E. L. & Biggerstaff, M. I. 1986 Onset of surface-tension-driven Bénard convection. *J. Fluid Mech.* **167**, 49–64.

Koschmieder, E. L. & Pallas, S. G. 1974 A sensor for heat transfer measurements. *Rev. Sci. Instrum.* **45**, 1164–1165.

Koschmieder, E. L. & Prahl, S. A. 1990 Surface-tension-driven Bénard convection in small containers. *J. Fluid Mech.* **215**, 571–583.

Koschmieder, E. L. & Switzer, D. W. 1992 The wavenumber of supercritical surface-tension-driven Bénard convection. *J. Fluid Mech.* **240**, 533–548.

Koschmieder, E. L. 1993 *Bénard Cells and Taylor Vortices*. Cambridge University Press.

Krishnamurti, R. 1970 On the transition to turbulent convection. Part 2. The transition to time-dependent flow. *J. Fluid Mech.* **42**, 309–320.

Le Gal, P., Pocheau, A. & Croquette, V. 1985 Square versus roll pattern at convective threshold. *Phys. Rev. Lett.* **54**, 2501–2504.

Malkus, W. V. R. & Veronis, G. 1958 Finite amplitude cellular convection. *J. Fluid Mech.* **4**, 225–260.

Merzkirch, W. 1974 *Flow Visualization*. Academic.

Mindlin, G. B., Ondarçuhu, T., Mancini, H. L., Pérez-García, C. & Garcimartín, A. 1994 Comparison of data from Bénard–Marangoni convection in a square container with a model based on symmetry arguments. *Intl J. Bifurcation Chaos* **4**, 1121–1133.

Morris, S. W., Bodenschatz, E., Cannell, D. S. & Ahlers, G. 1993 Spiral defect chaos in large aspect ratio Rayleigh–Bénard convection. *Phys. Rev. Lett.* **71**, 2026–2029.

Moses, E. & Steinberg, V. 1986 Competing patterns in a convective binary mixture. *Phys. Rev. Lett.* **57**, 2018–2021.

Nield, D. A. 1964 Surface tension and buoyancy effects in cellular convection. *J. Fluid Mech.* **19**, 341–352.

Nitschke-Eckert, K. & Thess, A. 1995 Secondary instability in surface-tension-driven Bénard convection. *Phys. Rev.* E **52**, R5772–R5775.

Oliver, D. S. 1983 Planform of convection with strongly temperature-dependent viscosity. *Geophys. Astrophys. Dyn.* **27**, 73–85.

Ondarçuhu, T., Millán-Rodrígues, J., Mancini, H. L., Garcimartín, A. & Pérez-García, C. 1993 Bénard–Marangoni-convective pattern in small cylindrical layers. *Phys. Rev.* E **48**, 1051–1057.

Palmer, H. J. & Berg, J. C. 1971 Convective instabilities in liquid pools heated from below. *J. Fluid Mech.* **47**, 779–787.

Pampaloni, E., Pérez-García, C., Albavetti, L. & Ciliberto, S. 1992 Transition from hexagons to rolls in convection in fluids under non-Boussinesq conditions. *J. Fluid Mech.* **243**, 393–416.

Parmentier, P. M., Regnier, V. C. & Lebon, G. 1996 Non-linear analysis of coupled gravitional and capillary thermoconvection in thin liquid layers. *Phys. Rev.* E **54**, 411–423.

Pearson, J. R. A. 1958 On convection cells induced by surface tension. *J. Fluid Mech.* **4**, 489–500.

Regnier, V., Dauby, P. C., Parmentier, P. & Lebon, G. 1997 Square cells in gravitional and capillary thermoconvection. *Phys. Rev.* E **55**, 6860–6865.

Scanlon, J. W. & Segel, L. A. 1967 Finite-amplitude cellular convection induced by surface tension. *J. Fluid Mech.* **30**, 149–162.

Schatz, M. F., Van-Hook, S. J., McCormick, W. D., Swift, J. B. & Swinney, H. 1995 Onset of surface-tension-driven Bénard convection. *Phys. Rev. Lett.* **75**, 1938–1941.

Siggia, E. D. 1994 High Rayleigh number convection. *Ann. Rev. Fluid Mech.* **26**, 137–168.

Simanovskii, I. B. & Nepomnyashchy, A. A. 1993 *Convective Instabilities in Systems with Interface*. Gordon and Breach.

Thess, A. & Bestehorn, M. 1995 Planform selection in Bénard–Marangoni-convection: l-hexagons versus g-hexagons. *Phys. Rev.* E **52**, 6358–6367.

Thess, A. & Orszag, S. A. 1995 Surface-tension-driven Bénard convection at infinite Prandtl number. *J. Fluid Mech.* **283**, 201–230.

Thiele, U. & Eckert, K. 1997 Stochastic geometry of polygonal networks – an alternative approach to the hexagon-square-transition in Bénard convection. *Phys. Rev.* E (submitted).

Velarde, M. G. & Castillo, J. L. 1982 Transport and reactive phenomena leading to interfacial instability. In *Convective Transport and Instability Phenomena* (ed. J. Zierep, H. Oertel, jr. & G. Braun).

Walden, R. W. & Ahlers, G. 1981 Non-Boussinesq and penetrative convection in a cylindrical cell. *J. Fluid Mech.* **109**, 89–114.

White, D. B. 1988 The planforms and onset of convection with a temperature-dependent viscosity. *J. Fluid Mech.* **191**, 247–286.

Whitehead, J. A. & Parsons, B. 1978 Observations of convection at Rayleigh numbers up to 760 000 in a fluid with large Prandtl number. *Geophys. Astrophys. Fluid Dyn.* **9**, 201–217.

Yu, S.-T., Jiang, B.-N. & Duh, J. C. 1996 Three-dimensional simulation of Marangoni–Bénard convection in small containers by least-square finite element method. *AIAA Paper* 96-0863.